**NASA
Technical
Paper
2270**

February 1984

Theoretical and Experimental Engine-Inlet Flow Fields for Fighter Forebodies

Steven F. Yaros

NASA

NASA Technical Paper 2270

1984

Theoretical and Experimental Engine-Inlet Flow Fields for Fighter Forebodies

Steven F. Yaros

Langley Research Center
Hampton, Virginia

National Aeronautics
and Space Administration

**Scientific and Technical
Information Branch**

INTRODUCTION

The study of airframe and engine-inlet integration has recently become even more important in the light of current fighter and supercruiser aircraft design. These configurations are characterized by fuselages and canopies with distinctly nonaxisymmetric cross-sectional geometries and thin, low-aspect-ratio, highly tapered swept wings. Inlet external surfaces are often well integrated with the fuselage (ref. 1), and the inlets may be located almost anywhere on the fuselage (ref. 2). Such aircraft configurations may also include, in more complicated cases, forward-mounted canards, wing strakes, leading-edge extensions (LEX's), fins, and stores hung in a multitude of combinations.

Inlet performance is determined to a great extent by the flow field just ahead of the inlet entrance plane. Satisfactory inlet performance usually requires that flows at the inlet face be high in total-pressure recovery and that this recovery and the local flow inclination be relatively insensitive to aircraft flight conditions.

The effects of these configuration parameters on the flow into the inlet are many. The inlet is subject to a number of disturbances from the aircraft forebody alone, including large flow variations, substantial boundary-layer growth, vortex shedding, and shock impingement. If the inlet is shielded by the wing of the aircraft, further complications may arise through the complex interaction between the wing and forebody, the effects of which are highly three-dimensional. In such cases it is usually possible to adjust the inlet location and the wing position to optimize inlet performance, but not without sacrifices. For example, burying the inlet well behind the leading edge of the wing near the fuselage will almost certainly improve the inlet performance at high angles of attack, but usually at the expense of performance at substantial angles of sideslip (ref. 3).

Other contributors to aircraft inlet flow problems are the various protuberances that are placed on the aircraft fuselage or wings. Canopies, LEX's, and canards, in their traditional positions, cause the most serious problems for engine inlets at high angles of attack or sideslip or both (ref. 4). Low- or side-mounted inlets are more likely to be disturbed by stores hung from the fuselage or wing or by ventral fins, although the latter are usually placed far enough aft to be no problem.

The purpose of this study was to assess the capability of two numerical flow prediction methods to predict forebody flow fields near the engine inlet on realistic fighters. For this study only inviscid prediction methods were considered. The target of this study was to determine the shortcomings of these methods, which could not be expected to predict viscous effects. The fighter speed range from Mach 0.9 to 2.5 and angles of attack from 0° to 25° were of interest, and of prime importance was the realistic modelling of the aircraft geometry. The ease of use of the computer programs that implemented each method and their economy of operation was also considered.

Predictions of aircraft forebody flows are valuable not only to the designer but also to the wind tunnel test engineer (ref. 5). The results are presented in a form particularly useful to both, namely, flow-field contours, at the hypothetical inlet entrance plane, of local angle of attack, angle of sideslip, and Mach number.

Two other subjects, which will not be included in this investigation, must be mentioned in the interest of completeness: cyclic flow distortion and spillage. The first phenomenon may have a strong adverse effect on inlet pressure recovery, particularly during maneuvering flight (ref. 6), and is extremely configuration dependent. Inlet spillage, because of its deformation of the aircraft flow field, can seriously affect the aerodynamic efficiency of the aircraft. Recent theoretical predictions of this phenomenon have agreed well with wind tunnel data (ref. 7).

SYMBOLS

c_p	specific heat at constant pressure
c_v	specific heat at constant volume
M	Mach number
P	ln p
p	pressure (normalized with respect to $\bar{p}_\infty$)
S	entropy (normalized with respect to $\bar{c}_{v,\infty}$)
T	temperature (normalized with respect to $\bar{T}_\infty$)
u,v,w	velocities corresponding to the x, y, and z directions (normalized with respect to $\sqrt{\bar{p}_\infty/\bar{\rho}_\infty}$)
x,y,z	Cartesian coordinates in the axial, transverse, and normal directions (normalized with respect to an arbitrary length)
α	angle of attack, $\tan^{-1}(w/u)$
β	angle of sideslip, $\tan^{-1}(v/u)$
γ	ratio of specific heats, $\bar{c}_p/\bar{c}_v$
ρ	density (normalized with respect to $\bar{\rho}_\infty$)
ϕ	perturbation potential function

Subscripts:

l	local conditions
∞	free-stream conditions
x,y,z	partial derivatives with respect to the appropriate direction or directions

A bar over a symbol indicates a dimensional value.

NUMERICAL PREDICTION METHODS

Because of the differences in the simplified equations of motion for supersonic and transonic flows, almost all the numerical methods investigated were specifically for one speed regime or the other. During the course of this study, certain criteria were used to assess the applicability of each of the computer programs. Solution accuracy, integrity of the geometric model, operational ease, and running expense were the most important criteria. In the final analysis, for supersonic cases, a three-dimensional Euler equation marching code, STEIN, was chosen over a surface paneling code, the PAN AIR Pilot Code. Although the latter program was applicable to a wide range of geometric configurations and had reached a high level of technical development (ref. 8), recent studies (ref. 9) have shown that it is less accurate relative to the STEIN code and is substantially more expensive to operate.

A similar situation developed in the search for a transonic code. Ultimately, a small-disturbance code, WIBCO, was chosen over a full-potential code, FLO-30, which is the latest member of a family of FLO-codes (refs. 10 to 12), each of which is capable of handling a more complex wing-body configuration. Investigation of the most recent FLO-30 calculations (ref. 13), however, indicated that the method by itself was capable of solutions for fuselages of only moderate complexity, particularly if the wing was of low aspect ratio. Since many of the fighter cross sections varied considerably from an axisymmetric shape, it was decided that WIBCO would be the better choice, in spite of the small-disturbance approximations applied in the calculations.

Although neither WIBCO nor STEIN had been developed for application to fighter aircraft configurations, it was anticipated that modifications to the codes as might be necessary could be efficiently carried out because of their usage in many areas and the availability of complete documentation.

One other factor weighed heavily in the choice of the STEIN and WIBCO codes: the similarity of the aircraft model geometry input. Both codes have slightly different versions of the QUICK-geometry methodology developed by Vachris and Yaeger (ref. 14). In this method the aircraft cross sections are described at appropriate stations by specifying control points at each cross section and the type of curves to be used to connect the points. After the details of each cross-sectional geometric model are specified, the aircraft body lines are described in a manner similar to the cross sections, piece by piece, with lines, ellipses, parabolas, and so forth. The result is an analytical body model that allows a quick calculation of surface points and slopes over the entire length of the body. This method requires the body coordinates to be single-valued polar coordinates. The wing, if present, is considered as an outgrowth of the body for the STEIN input, whereas the wing is a separate specification of chord sections at different span locations for the WIBCO input.

The task of describing the aircraft geometry by this method can become time consuming. It was eased substantially for the present study through the availability of an interactive graphics system developed by Adams (ref. 15). Examples of the use of this system in defining a typical fuselage cross section and a body line are shown in figure 1(a). The resulting geometric model, plotted as a series of cross sections, is shown in figure 1(b).

Supersonic Code - STEIN

According to reference 16, STEIN was originally formulated to provide inviscid solutions for flows in supersonic or hypersonic conditions for a wide variety of vehicle configurations throughout a large angle-of-attack range. All forms of small-perturbation techniques, valid only at low Mach numbers and low angles of attack, and

Newtonian theory, valid only at high Mach numbers, were rejected as being inadequate for the problems at hand. Thus, STEIN was developed as a finite-difference marching solution of the three-dimensional Euler equations with shock-fitting techniques applied to selected types of shocks. Marching solutions carry an implicit requirement that the flow throughout the field of interest be supersonic. As will be seen, this requirement affects the range of Mach numbers and the type of configurations for which the STEIN code is applicable.

The geometric model that is input to the code is in the QUICK-geometry format. Wings, canards, and other protuberances are defined simply as outgrowths from the fuselage shape at each cross section. The input that the code requires as well as a summary of the QUICK-geometry system are presented in reference 17.

The solution "marches" along an axis of the vehicle from a starting solution near the nose toward the tail of the aircraft. Two options are allowed for the starting solution, one for a blunt nose and one for a pointed nose. The fighter aircraft in this study were configured with pointed noses, and thus the second option was used. A conical supersonic flow is assumed up to a certain fuselage station, the "starting plane," beyond which the marching solution takes over. Downstream from the starting plane, the region of computation is bounded by the body and by the bow shock of the vehicle. This area is first transformed, conformally, to a mapped space in which the geometric cross sections become "near circles." The computational space is formed from the mapped space by normalizing the radial and circumferential distances between the body and the bow shock, with the portions of the plane of symmetry above and below the aircraft becoming the upper and lower limits of the computational mesh. The normalization results in a rectangular computational grid which transforms into a grid in the physical space that is finely spaced in regions of highly convex body curvature.

Shocks that form within the computational grid are considered to be of two types: "cross-flow" shocks, which are predominantly radial, and "wing" or "canopy" shocks, which are essentially at a constant radius in the mapped plane. Figure 2 shows a typical shock configuration generated by a winged aircraft in which there are bow, canopy, and wing shocks. All these imbedded shocks are located by monitoring local pressure throughout the flow and determining the point of maximum gradient based on a cubic polynomial curve fit. Locations of inverse pressure gradients arbitrarily near zero are designated as shock points. The transformation from the mapped to the computational space is then adjusted so that the shocks become mesh lines, with the Rankine-Hugoniot relation being applied across each shock. As the code progresses downstream, each shock wave is followed until its demise or until it merges with another shock. A typical representation of the mesh as it appears in the physical plane is shown in figure 3. Note the manner in which the canopy and wing shocks are fitted into the mesh between the body and bow shock, ensuring that the shock locations are single valued throughout all the planes.

In regions of continuous flow, the Euler equations in the physical plane in a marching form are

$$uP_x + \gamma u_x = -(vP_y + w_z P + \gamma v_y + \gamma w_z) \tag{1}$$

$$uv_x = -(vv_y + wv_z + TP_y) \tag{2}$$

$$uw_x = -(vw_y + ww_z + TP_z) \tag{3}$$

$$TP_x + uu_x = -(vu_y + wu_z) \tag{4}$$

$$uS_x = -(vS_x + wS_z) \tag{5}$$

with a corresponding ideal-gas equation of state

$$\ln T = \frac{\gamma - 1}{\gamma} P + \frac{1}{\gamma} S \tag{6}$$

Upon transformation to the computational plane, the derivatives of the five dependent variables P, u, v, w, and S appearing on the right-hand sides of the equations are evaluated explicitly, and the solution is stepped by using a MacCormack two-level predictor-corrector scheme (ref. 16). This procedure is varied at body and shock points. Use of the MacCormack scheme and strict control of the step size ensures second-order accuracy in the marching direction for a linear system of equations, and truncation error is assumed correspondingly small for the present system.

The version of the STEIN code used herein includes the most recent modifications to the capabilities of STEIN (ref. 18): inlet mass ingestion, subsonic axial Mach number, improved conformal mappings, and sideslip. Only the second and third modifications were used in this study.

Transonic Code - WIBCO

The WIBCO transonic code was developed by Boppe (ref. 19) primarily to apply the solution of the small-disturbance potential equation to arbitrary wing and body geometries. Recognizing the increasing complexity of traditional grid transformations as configurations become more three-dimensional, Boppe avoids these problems by imbedding fine Cartesian grids into an overall coarse grid in regions where more flow detail is required. The concept is shown schematically in figure 4 for wing and body fine grids imbedded in the global crude grid. The crude grid in the physical space is stretched in all directions to infinity (except at the plane of symmetry) according to the method of reference 20. Stretching in the z-direction is also proportional to the tangent function, whereas in the y-direction the function of choice is the hyperbolic tangent.

The wing and body fine-grid systems are constructed to totally encapsulate their portions of the geometry and to provide computations over a much smaller area of the flow. These two fine-grid systems overlap and transfer information to each other, as well as to the crude-grid system, during the course of the iterations. It should be noted that although the body fine-grid system is a regular Cartesian grid, the wing fine-grid system is swept and tapered according to the planform shape.

The geometry system used for WIBCO is the same as that used for the STEIN supersonic code, with two differences: first, WIBCO uses QUICK-geometry only for the body and with several options removed; and second, the wing is defined separately as wing sections at different span stations. Once these two limitations are considered, however, a careful design of the STEIN geometry can be transferred with only minor changes to be used as WIBCO input.

The small-disturbance equation used in WIBCO, including three terms that are usually present only in the full-potential representation, is

$$\left[1 - M_\infty^2 - (\gamma + 1)M_\infty^2\phi_x - \frac{\gamma + 1}{2} M_\infty^2\phi_x^2\right]\phi_{xx} - 2M_\infty^2\phi_y\phi_{xy}$$

$$+ \left[1 - (\gamma - 1)M_\infty^2\phi_x\right]\phi_{yy} + \phi_{zz} = 0 \tag{7}$$

The $\phi_y\phi_{xy}$ and $\phi_x\phi_{yy}$ terms are included to facilitate the resolution of shock waves on wings of large sweep angles, and the $\phi_x^2\phi_{xx}$ term is included to provide a better indication of when the equation changes type from elliptic to hyperbolic and vice versa.

The finite-difference approximations are straightforward. Central differencing is used throughout except in areas of local supersonic flow, in which upwind differencing is used for most of the second derivative terms. In keeping with the near-isentropic nature of the flow, nonconservative difference operators are used, although it is acknowledged that results will become less accurate with increasing shock strength. For a wing-body configuration, the solution begins with an arbitrary number (typically 100) of successive line-overrelaxation sweeps of the crude grid to provide a starting solution for the fine-grid systems. The second phase of the solution involves a sweep of the wing fine-grid, the body fine-grid, and the crude-grid system with appropriate updating of overlapping areas. Approximately 80 second-phase iterations are usually required. Since none of the grid systems are body or wing fitted, boundary conditions are applied at mesh points nearest the actual surfaces. Corrections are applied at these points for wing-surface slope and body displacement as well as for local flow inclination.

The version of WIBCO used herein is the basic wing-body code. Further capabilities have been added (ref. 21), including the fine-grid system applied to pylons, nacelles, and winglets, as well as a scheme for modelling inlet spillage and exhaust interference effects.

EXPERIMENTAL DATA

One of the problems in obtaining good inlet flow-field data for realistic aircraft forebodies is the sheer size of the models necessary to provide sufficient geometric detail. The problem is made much worse if flow-field studies are extended to high angles of attack and sideslip. At least one imaginative method has been tested (ref. 22) to provide realistic inclined flow to an inlet while eliminating the need for a massive forebody model in the wind tunnel. On the other hand, a great amount of data on large models was obtained in the early 1970's in Project Tailor-Mate, a study of various aircraft forebody shapes and their effects on engine-inlet flows. The first part of the project, which was specifically concerned with forebody-alone flow fields, provided the data used for comparisons herein. These forebody tests were performed without engine-inlet simulators on wing-body combinations representative of three types of fighter aircraft inlet configurations: side-mounted, wing-shielded, and body-shielded.

The first two of these configurations are considered in this paper, and sketches of the full aircraft configurations are shown in figure 5. It was felt the third configuration would not be as challenging as the first two. The supersonic and transonic wind tunnel tests were performed in the 16S and 16T wind tunnels at AEDC (refs. 23 to 25). The actual tests used in this report were run without engine nacelles. Three types of data were taken during the forebody tests: cone-probe flow-field data, body pressure data, and boundary-layer data. The predictions in this paper are concerned only with the forebody flow field near the inlet. Thus, comparisons are made with the first type of data and are presented in a format offering direct comparison with the data in references 23 to 25.

The tests were run at Mach numbers of 0.9 to 2.50 and at angles of attack of -5° to 25°. Although the quality of the data is considered to be very good, post-test examination of the cone-probe data (ref. 26) has indicated that one of the five cone probes was faulty. On examination of the original tabulated data, it was decided to omit data from this probe. Surber and Sedlock (ref. 26) estimate the data from the other probes to be accurate to ±1°. One other problem was the lack of detailed drawings of the aircraft configurations. As a result, the numerical models generated for this study were based on rather small scale cross sections presented in references 23 to 25. However, the inaccuracies thus introduced appear to be no greater than those introduced by the approximations made in defining the aircraft geometry analytically, as required by the STEIN and WIBCO codes.

RESULTS AND DISCUSSION

A partial summary of the results herein is presented in reference 27. The results of this paper are summarized in table 1.

Side-Mounted Inlet Configuration

The fuselage geometry generated with the STEIN code for the side-mounted inlet configuration (fig. 5) is shown in figure 6. The density of the circumferential grid was increased about halfway down the fuselage, as was the density of the radial grid (not shown in the figure), in order to provide a more detailed mesh in the region of the inlet. The WIBCO model, being specified by the same QUICK-geometry as the STEIN model, was very similar to the model in figure 6, with the density of points in the body-fine grid system tending to be higher than those of the STEIN model over the entire body.

Representative cases for the STEIN code were chosen to be those at $M_\infty = 2.5$. Solutions were successful at this Mach number for angles of attack up to 15°, as shown in figures 7 to 10. These figures show comparisons of predicted and experimental contours of local angle of attack, local angle of sideslip, and local Mach number. Beyond $\alpha = 15°$, the inclination at the nose of the aircraft was too high for the conical flow starting solution to be successful, indicating that the actual flow contained a detached bow shock. It is conceivable that a blunt-nose starting solution would be capable of overcoming this difficulty, but that approach was not attempted in this study.

Examination of figures 7 to 10 shows that both the predictions and the experimental data behaved consistently as the angle of attack was increased from 0° to 15°. The agreement of the prediction and the experimental data of the flow inclinations is good, whereas the agreement between Mach numbers is consistently poor. The theoretical local angle of attack is consistently 1° high, and the theoretical local angle of sideslip is consistently 1° low (inboard), perhaps reflecting the estimated ±1° probe accuracy stated previously.

When the Mach number was lowered, the STEIN code was capable of producing a good flow solution at $M_\infty = 2.2$ and $\alpha = 0°$ and (fig. 11), which compared as favorably with experimental data as the $M_\infty = 2.5$ solution (fig. 7). No solution at $M_\infty = 1.6$, even at $\alpha = 0°$, was possible, however, as the configurations and flight conditions once again produced a detached bow shock.

Similar good results were obtained with the WIBCO code in the transonic case, shown in figures 12 to 17. In general, local angles of attack and sideslip agreed to within a couple of degrees, with discrepancies growing as the angle of attack increased to $\alpha = 25°$. At this highest angle of attack (see fig. 17(b)), the β_l contours show that in the experiment the flow showed a much stronger outflow on the lower (windward) side of the body and a much weaker inflow on the upper (leeward) side of the body than the prediction, which can be taken as an indication of viscous effects and possible flow separation. This can be seen in the Mach number contours also (see fig. 17(c)), in which the experimental flows did not accelerate around the upper shoulder of the model as the inviscid prediction of the WIBCO code shows.

The WIBCO code was able to produce solutions for this configuration at low supersonic Mach numbers of 1.2, 1.4, and 1.6, and figure 18 shows the results at $M_\infty = 1.6$. Local flow angles show good agreement. A WIBCO solution at $M_\infty = 2.2$ (fig. 19), well above what is usually considered transonic flow, shows very good agreement with the experimental data and the STEIN results (fig. 11).

Wing-Shielded Inlet Configuration

Figure 20 shows the geometric model for the STEIN code for the wing-shielded inlet configuration. As before, the coordinate mesh density was increased about halfway down the model. The geometric description shown is one composed entirely of cross-section descriptions up to the area of interest. For the transonic cases, however, the overall sensitivity of the flow to a much longer portion of the aircraft geometry dictated a different geometric description. The aircraft model used for the WIBCO code was much longer, and the wing is described in its entirety as a spanwise sequence of cross sections. Attempts made to model the geometry in the same manner as for the supersonic case proved to be unsatisfactory.

The supersonic results of the STEIN code were obtainable only at $\alpha = 0°$ and 5° at $M_\infty = 2.5$ because of large subsonic areas near the wing-fuselage juncture. The results are shown as figures 21 and 22.

Shielding the inlet under the wing provides a substantial lessening of the effects of the local angle of attack, as can be seen from comparing figures 8(a) and 22(a). Although quantitative agreement of the inclinations does not seem to be very good, it is significant to note that angular variations are small, and minute changes in local flow angles can cause substantial changes in contour placement. Wind tunnel data obtained at a fuselage station slightly upstream of the station shown in figure 21(a) agree much better with the predicted contours even though the magnitudes of the angles involved are essentially the same. At angles of attack of 10° and above the STEIN code encountered difficulties. The problems occurred at the sharp leading edge of the wing, where a local two-dimensional flow solution is used for the shock wave. The flight conditions and the geometry of the wing called for a detached shock, a situation that was unattainable with the present algorithm. Modifications to the previously described shock-fitting scheme could possibly remedy this situation, as could the redefinition of the leading edge of the wing as blunt. The results at $\alpha = 5°$ are reasonable, with discrepancies near the body attributable once again to inaccuracies in the geometric description and lack of viscous capability in the prediction code. No solutions were possible for this configuration for Mach numbers of 2.2 or below.

The WIBCO code, run for cases at $M_\infty = 0.9$, was more successful at the higher angles of attack. Results presented in figures 23 to 26, for angles of attack from 0° to 15°, show the flow patterns developing consistently. Qualitative agreement with the data is reasonable, with flow inclination errors on the order of 3° maximum at the highest angle of attack. As in previous cases shown for both configurations, both geometric modelling and viscous effects are responsible for discrepancies in the results. There is evidence of a large boundary layer moving from the fuselage to the lower surface of the wing, especially at the higher angles of attack.

Results of the WIBCO code at $\alpha = 0°$ for three higher Mach numbers (up to $M_\infty = 1.6$) are shown in figures 27 to 29. These figures and figure 23 show agreement of the local-flow-inclination contours for both the predictions and the experimental data.

CONCLUDING REMARKS

In general it may be said that the two inviscid numerical methods investigated in this paper were capable of predicting forebody flows to levels consistent with the preliminary design of engine-inlet locations. Comparisons of contours of local angles of attack, local angles of sideslip, and local Mach numbers were compared with wind tunnel data. The supersonic code, STEIN, showed a marked sensitivity to any development of subsonic regions, especially at low supersonic Mach numbers or at angles of attack greater than 5°. The transonic code, WIBCO, was more robust and was able to calculate reasonable solutions through the Mach number range of 0.9 to 1.6 at angles of attack of 15° and over, depending on configurations. Both codes require a fairly elaborate geometric input, which may become time consuming.

For aircraft inlet configurations more exotic than those considered, the two codes may not perform satisfactorily, particularly at high angles of attack or sideslip. Under such flight conditions, boundary layer build-up cannot be neglected even when the flow remains attached. This situation suggests that the next step in the analysis of such configurations should include viscous effects, including vortex shedding.

Langley Research Center
National Aeronautics and Space Administration
Hampton, VA 23665
January 2, 1984

REFERENCES

1. Surber, Lewis; Syberg, Jan; and Koncsek, Joseph: Performance of Highly Integrated Inlets for Supersonic Aircraft. Aerodynamics of Power Plant Installation, AGARD-CP-301, Sept. 1981, pp. 1-1 - 1-12.

2. Williams, T. L.; Hunt, B. L.; Smeltzer, D. B.; and Nelms, W. P.: Top-Mounted Inlet System Feasibility for Transonic-Supersonic Fighter Aircraft Applications. Aerodynamics of Power Plant Installation, AGARD-CP-301, Sept. 1981, pp. 2-1 - 2-17.

3. Surber, Lewis E.: Effect of Forebody Shape and Shielding Technique on 2-D Supersonic Inlet Performance. AIAA Paper No. 75-1183, Sept.-Oct. 1975.

4. Smeltzer, D. B.; Nelms, W. P.; and Williams, T. L.: Airframe Effects on a Top-Mounted Fighter Inlet System. AIAA J. Aircr., vol. 19, no. 12, Dec. 1982, pp. 1083-1087.

5. Surber, L. E.; and Stava, D. J.: Supersonic Inlet Performance and Distortion During Maneuvering Flight. Inlets and Nozzles for Aerospace Engines, AGARD-CP-91-71, Dec. 1971, pp. 25-1 - 25-18.

6. Kulfan, R. M.; and Sigalla, A.: Airframe-Propulsion System Aerodynamic Interference Predictions at High Transonic Mach Numbers Including Off-Design Engine Airflow Effects. Aerodynamics of Power Plant Installation, AGARD-CP-301, Sept. 1981, pp. 35-1 - 35-23.

7. Barton, J. M.: The Role of CFD in Aeropropulsion Ground Testing. AIAA-83-0149, Jan. 1983.

8. Ehlers, F. E.; Epton, M. A.; Johnson, F. T.; Magnus, A. E.; and Rubbert, P. E.: An Improved Higher Order Panel Method for Linearized Supersonic Flow. AIAA Paper 78-15, Jan. 1978.

9. Landrum, Emma Jean; and Miller, David S.: Assessment of Analytic Methods for the Prediction of Aerodynamic Characteristics of Arbitrary Bodies at Supersonic Speeds. AIAA-80-0071, Jan. 1980.

10. Caughey, D. A.; and Jameson, A.: Numerical Calculation of Transonic Potential Flow About Wing-Body Combinations. AIAA Paper No. 77-677, June 1977.

11. Caughey, David A.; Newman, Perry A.; and Jameson, Antony: Recent Experiences With Three-Dimensional Transonic Potential Flow Calculations. NASA TM-78733, 1978.

12. Caughey, D. A.; and Jameson, Antony: Recent Progress in Finite-Volume Calculations for Wing-Fuselage Combinations. AIAA Paper 79-1513, July 1979.

13. Verhoff, A.; and O'Neil, P. J.: Extension of FLO Codes to Transonic Flow Prediction for Fighter Configurations. Transonic Aerodynamics, David Nixon, ed., American Inst. Aeronaut. & Astronaut., Inc., c.1982, pp. 467-487.

14. Vachris, Alfred F., Jr.; and Yaeger, Larry S.: QUICK-GEOMETRY - A Rapid Response Method for Mathematically Modeling Configuration Geometry. Applications of Computer Graphics in Engineering, NASA SP-390, 1975, pp. 49-73.

15. Adams, Mary S.: Interactive Input for the QUICK Geometry System - User's Manual. NASA TM-81933, 1980.

16. Marconi, Frank; Salas, Manuel; and Yaeger, Larry: Development of a Computer Code for Calculating the Steady Super/Hypersonic Inviscid Flow Around Real Configurations. Volume I - Computational Technique. NASA CR-2675, 1976.

17. Marconi, Frank; and Yaeger, Larry: Development of a Computer Code for Calculating the Steady Super/Hypersonic Inviscid Flow Around Real Configurations. Volume II - Code Description. NASA CR-2676, 1976.

18. Marconi, Frank; and Koch, Frank: An Improved Supersonic, Three-Dimensional, External, Inviscid Flow Field Code. NASA CR-3108, 1979.

19. Boppe, Charles W.: Transonic Flow Field Analysis for Wing-Fuselage Configurations. NASA CR-3243, 1980.

20. Boppe, C. W.: Calculation of Transonic Wing Flows by Grid Embedding. AIAA Paper No. 77-207, Jan. 1977.

21. Boppe, C. W.; and Stern, M. A.: Simulated Transonic Flows for Aircraft With Nacelles, Pylons, and Winglets. AIAA-80-0130, Jan. 1980.

22. Palko, R. L.: A Method of Testing Full-Scale Inlet/Engine Systems at High Angles of Attack and Yaw at Transonic Velocities. AIAA Paper No. 72-1097, Nov.- Dec. 1972.

23. Cawthon, J. A.; Crosthwait, E. L.; Hill, P. W.; Lowery, B. T.; and Truax, P. P.: Supersonic Inlet Design and Airframe-Inlet Integration Program (Project Tailor-Mate). Volume 1 - Vehicle Conceptual Design and Performance Analysis. AFFDL-TR-71-124, Vol. 1, U.S. Air Force, May 1973. (Available from DTIC as AD 910 778L.)

24. Cawthon, J. A.; Crosthwait, E. L.; and Truax, P. P.: Supersonic Inlet Design and Airframe-Inlet Integration Program (Project Tailor-Mate). Volume 2 - Forebody Flow-Field Investigation. AFFDL-TR-71-124, Vol. 2, U.S. Air Force, May 1973. (Available from DTIC as AD 910 779L.)

25. Cawthon, J. A.; Truax, P. P.; and Steenkin, W. G.: Supersonic Inlet Design and Airframe-Inlet Integration Program (Project Tailor-Mate). Volume 3 - Composite Inlet Investigation. AFFDL-TR-71-124, Vol. 3, U.S. Air Force, May 1973. (Available from DTIC as AD 910 780L.)

26. Surber, Lewis E.; and Sedlock, Dennis: Analysis of Tailor-Mate Airframe-Inlet Flowfield Data and Inlet Performance Data for Supersonic Fighter Aircraft. AFFDL-TR-78-70, U.S. Air Force, Aug. 1978. (Available from DTIC as AD B032 622L.)

27. Yaros, Steven F.: Evaluation of Two Analytical Methods for the Prediction of Inlet Flow Fields in the Vicinity of Generalized Forebodies. AIAA-82-0959, June 1982.

TABLE 1.- SUMMARY OF SOLUTIONS

Configuration	Mach number	Code used and figure containing contours for angles of attack, deg, of —					
		0	5	10	15	20	25
Side-mounted	2.5	STEIN, fig. 7	STEIN, fig. 8	STEIN, fig. 9	STEIN, fig. 10		
	2.2	STEIN, fig. 11; WIBCO, fig. 19					
	1.6	WIBCO, fig. 18					
	0.9	WIBCO, fig. 12	WIBCO, fig. 13	WIBCO, fig. 14	WIBCO, fig. 15	WIBCO, fig. 16	WIBCO, fig. 17
Wing-shielded	2.5	STEIN, fig. 21	STEIN, fig. 22				
	1.65	WIBCO, fig. 29					
	1.4	WIBCO, fig. 28					
	1.2	WIBCO, fig. 27					
	0.9	WIBCO, fig. 23	WIBCO, fig. 24	WIBCO, fig. 25	WIBCO, fig. 26		

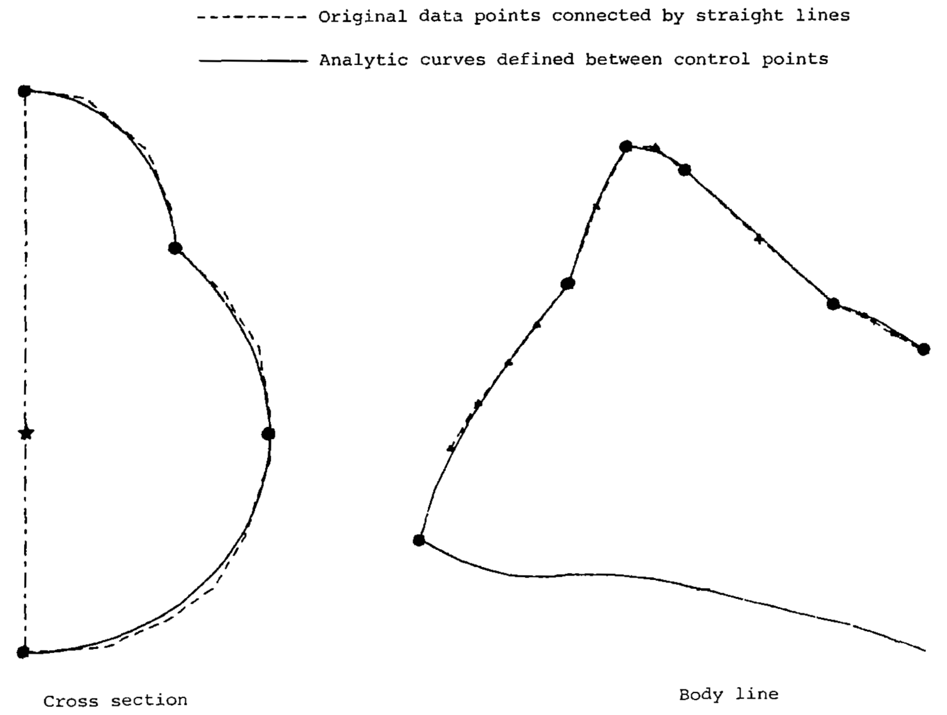

(a) Cross section and body line.

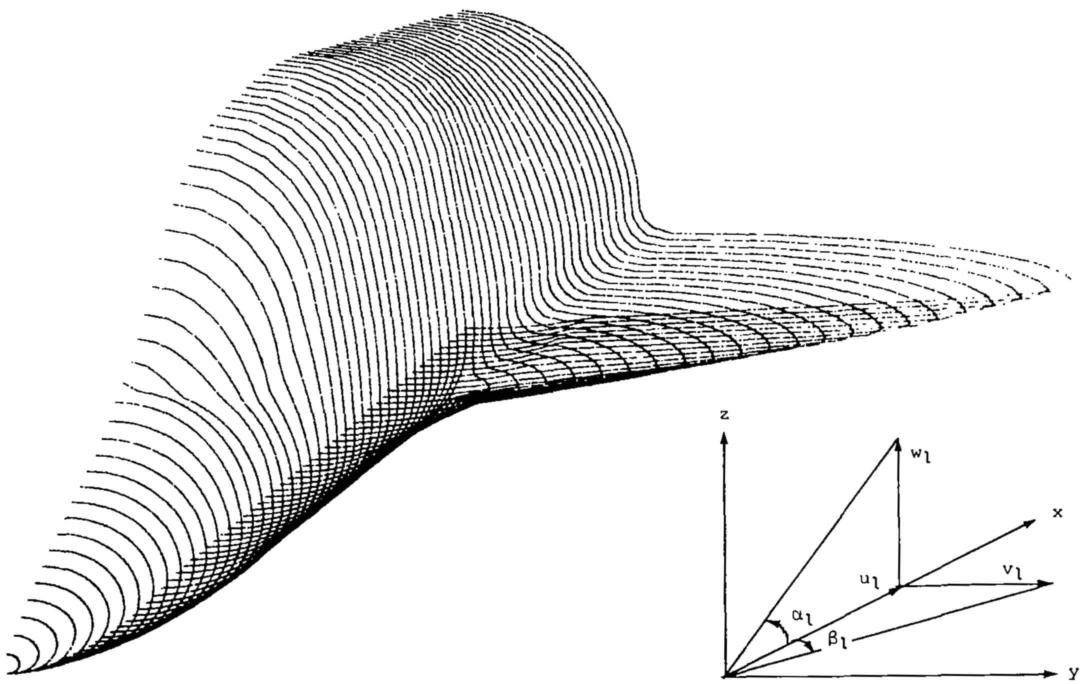

(b) Complete cross-section model.

Figure 1.- Typical QUICK-geometry body definition.

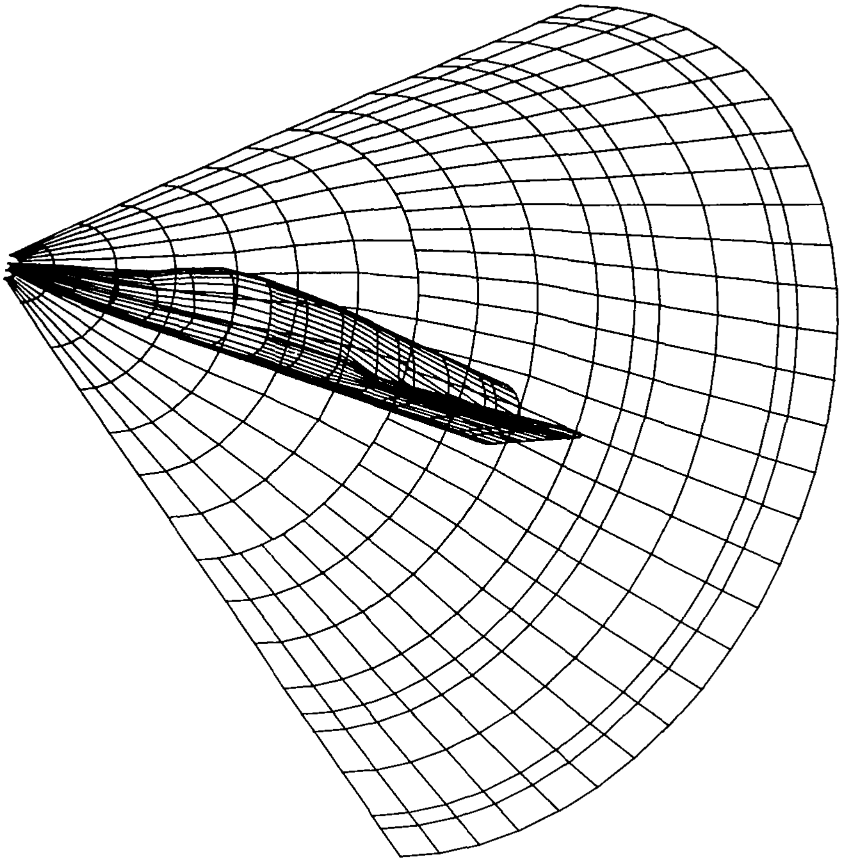

(a) Bow shock.

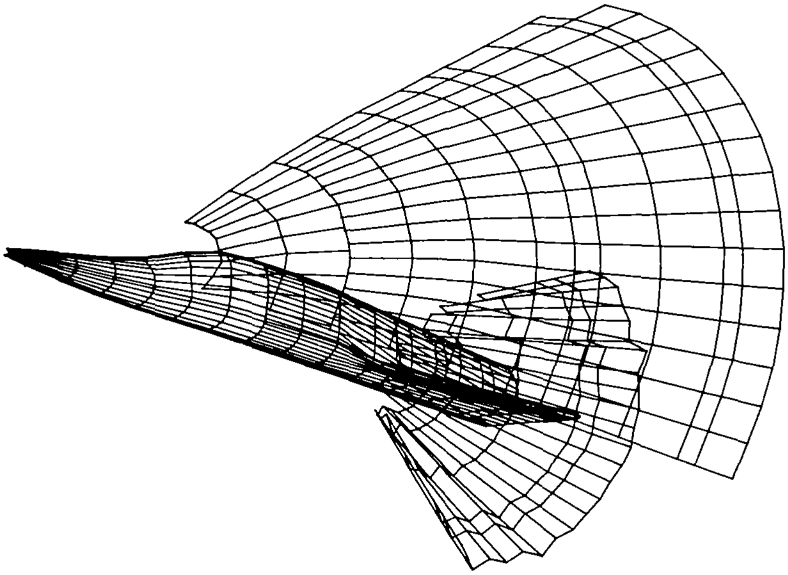

(b) Canopy and wing shocks.

Figure 2.- STEIN grid-shock development.

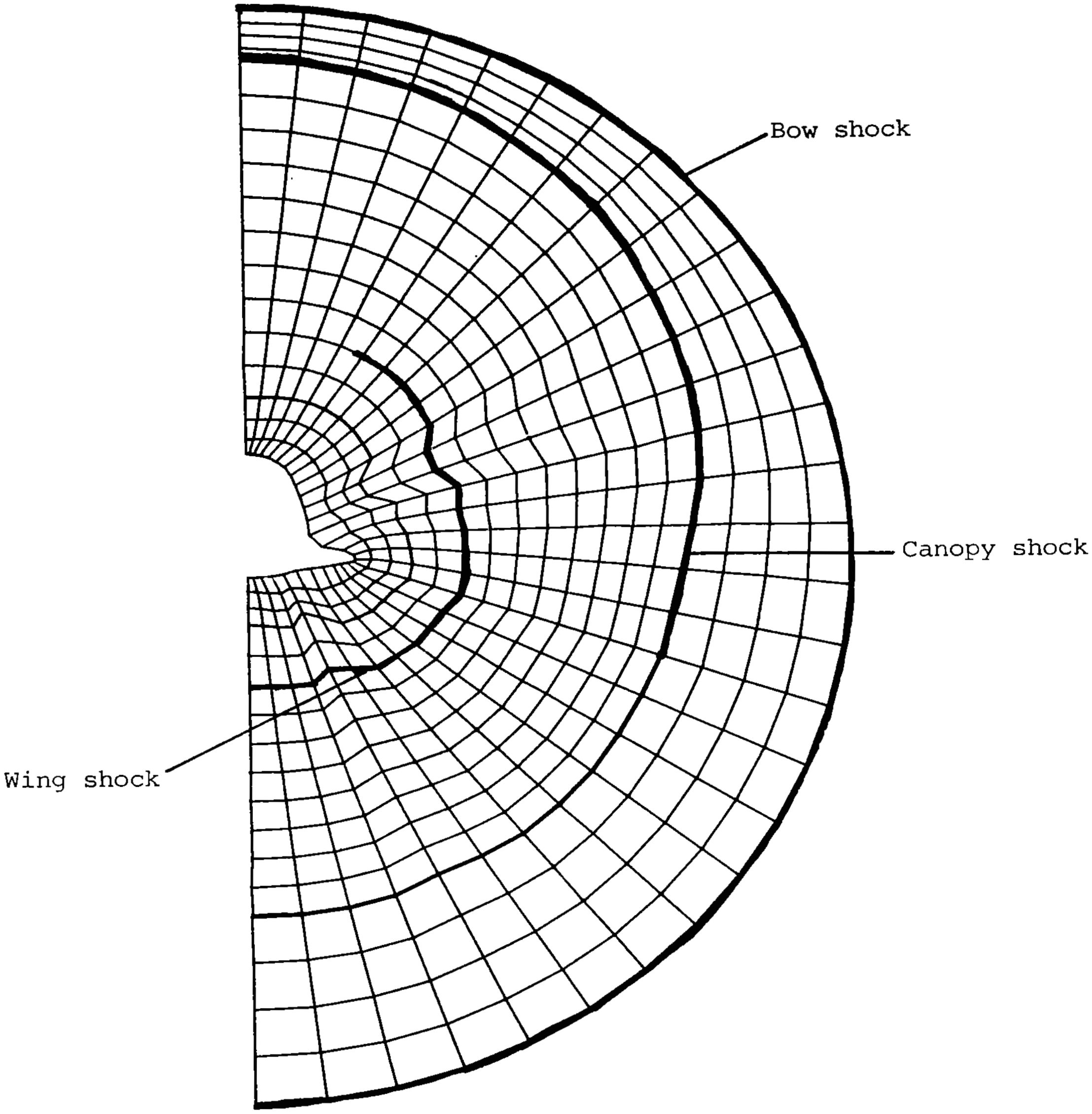

Figure 3.- STEIN cross-sectional grid pattern.

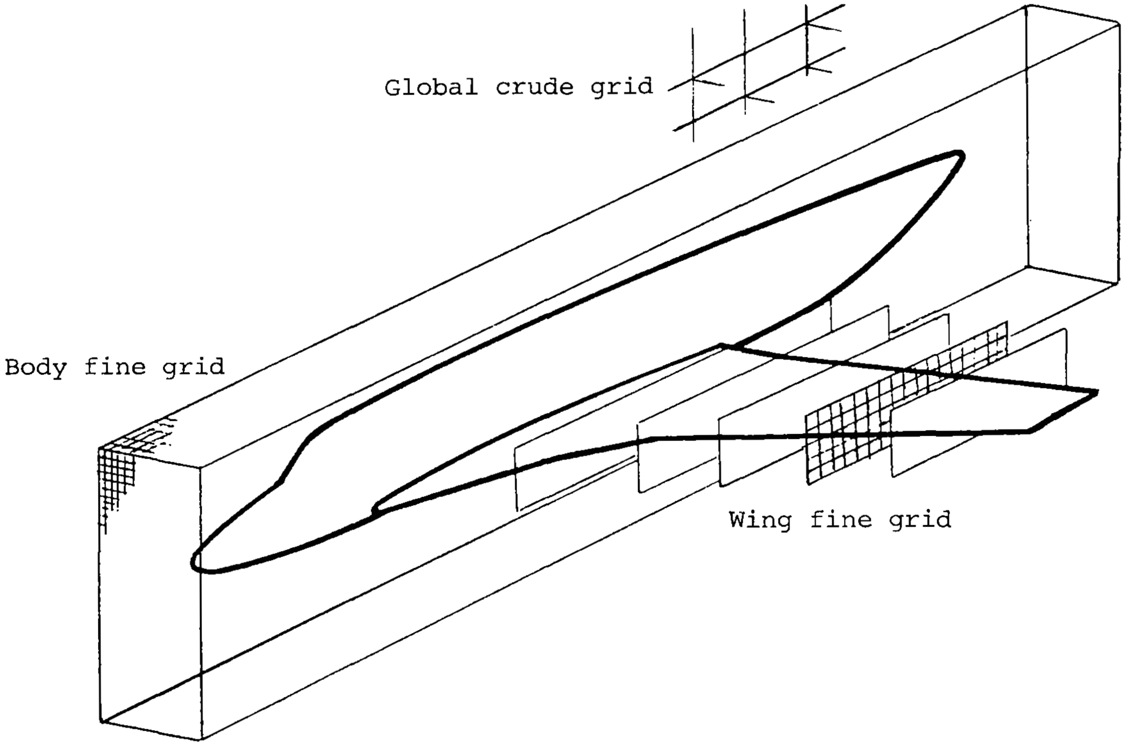

Figure 4.- WIBCO crude and fine grids. (From ref. 19.)

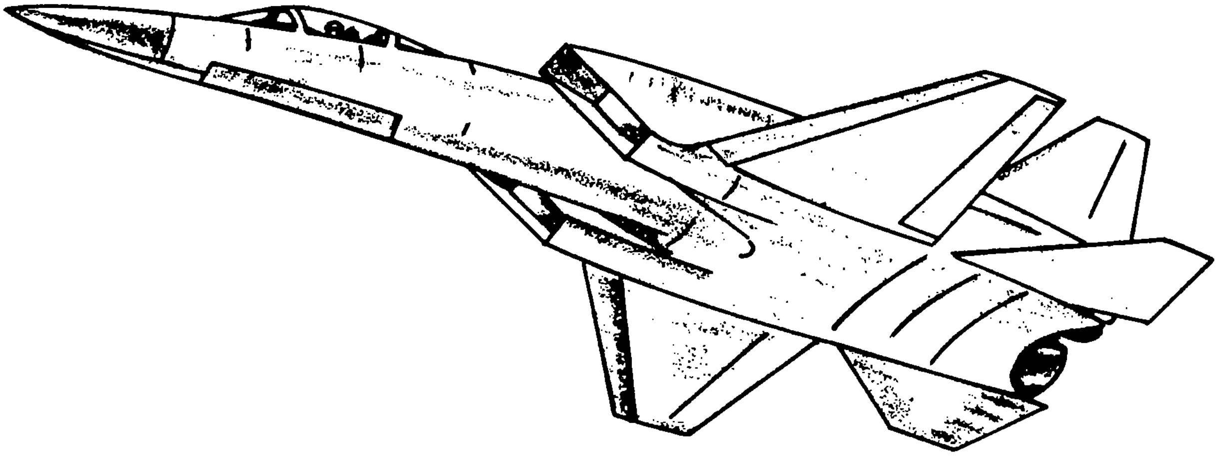

Side-mounted inlet

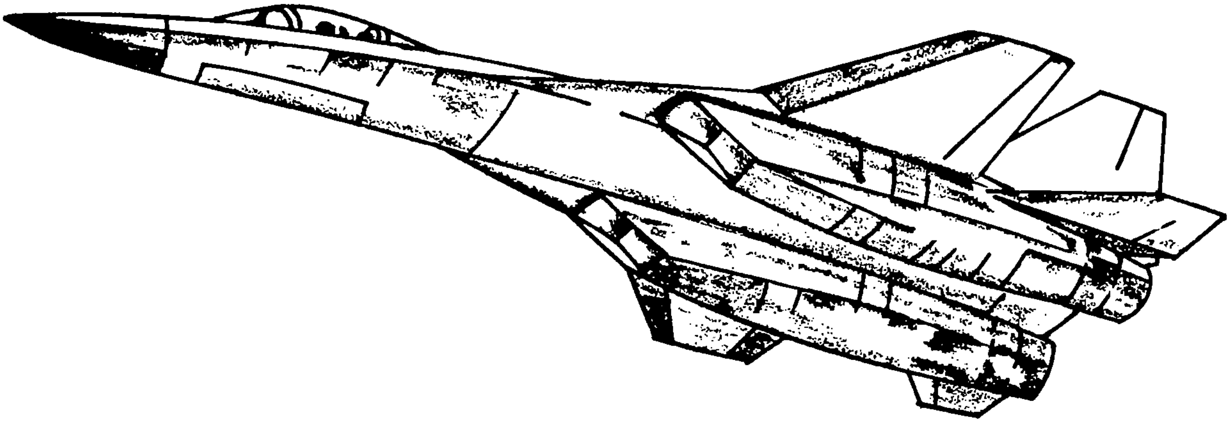

Wing-shielded inlet

Figure 5.- Project Tailor-Mate configurations.

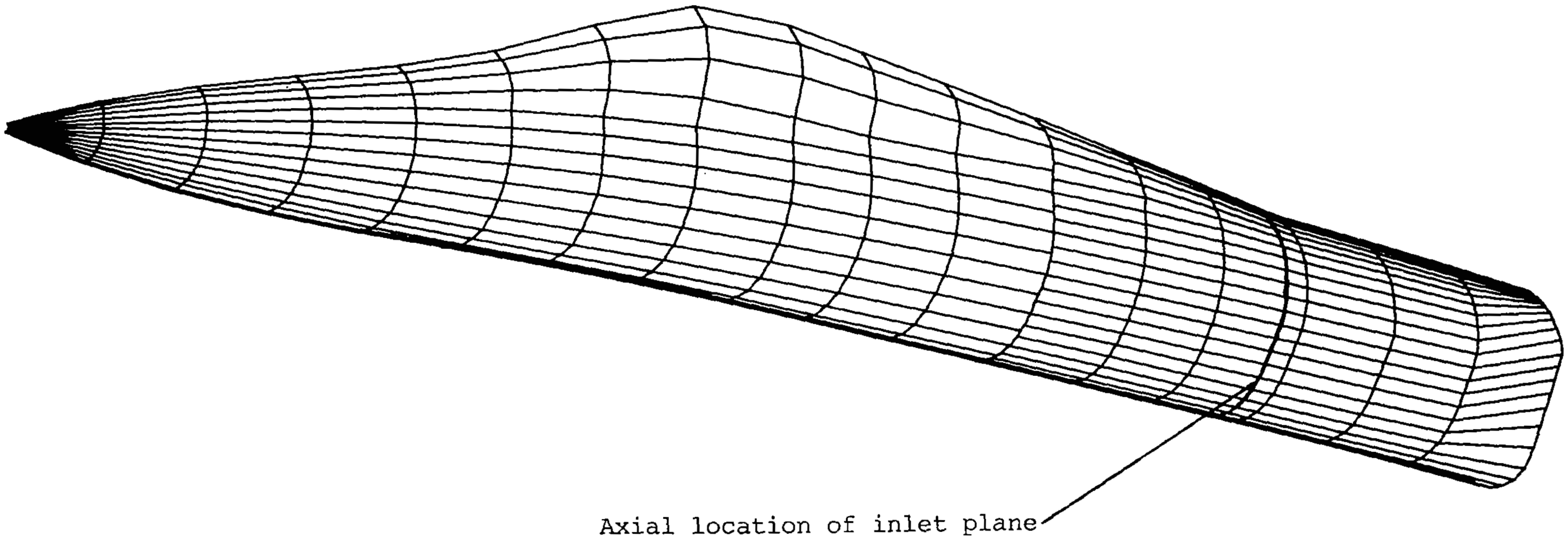

Figure 6.- QUICK-geometry model of Tailor-Mate side-mounted inlet configuration for use with STEIN code.

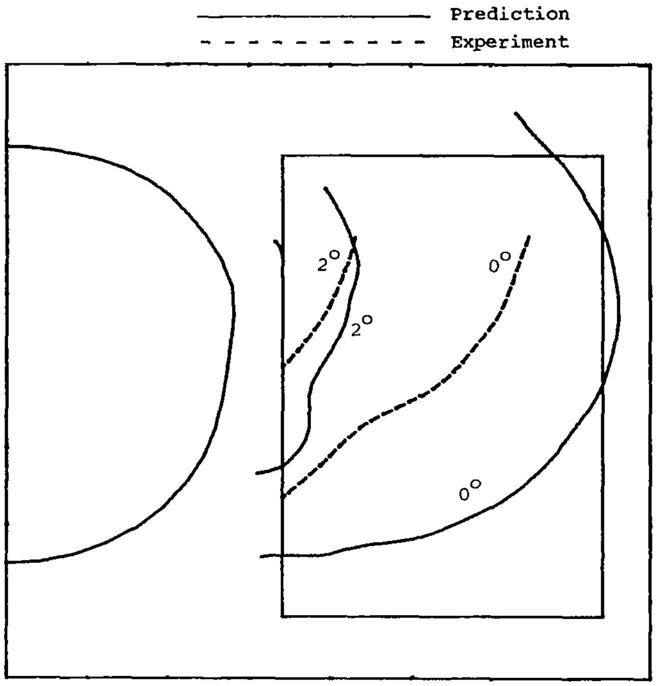

(a) α_l.

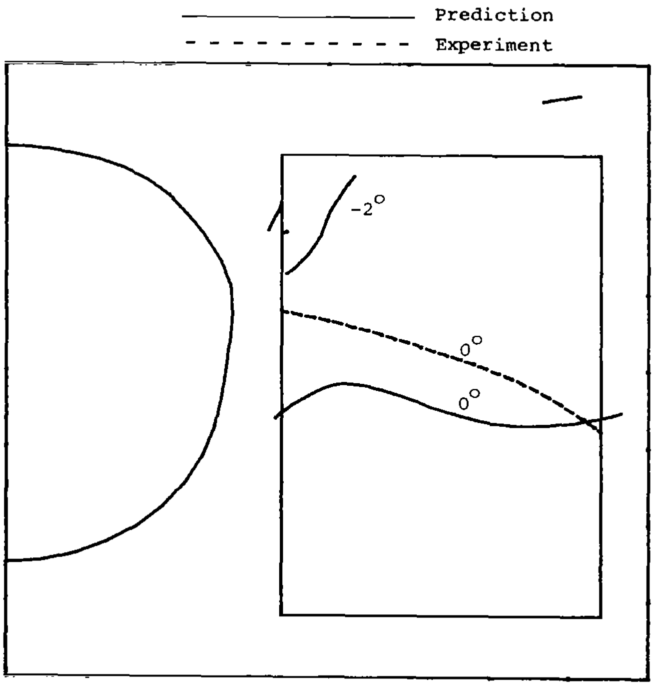

(b) β_l.

Figure 7.- Contours predicted from STEIN code and Tailor-Mate experimental data for side-mounted configuration at $M_\infty = 2.5$ and $\alpha = 0°$.

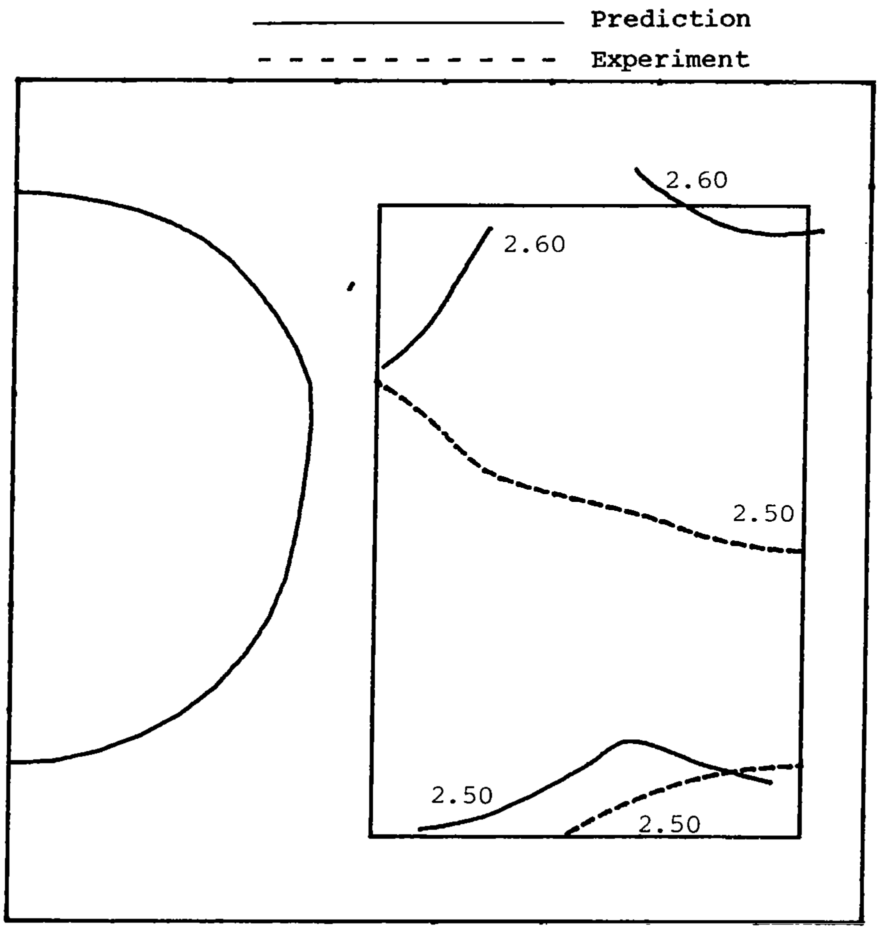

(c) M_l.

Figure 7.- Concluded.

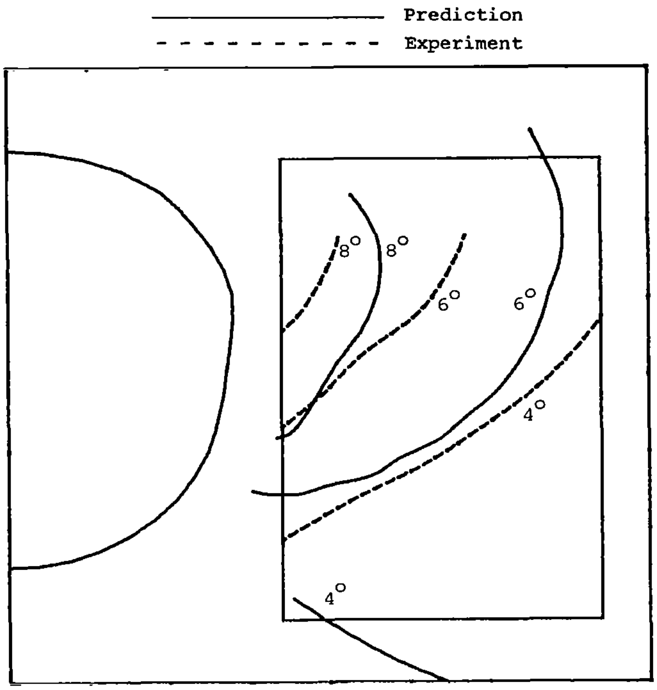

(a) α_l.

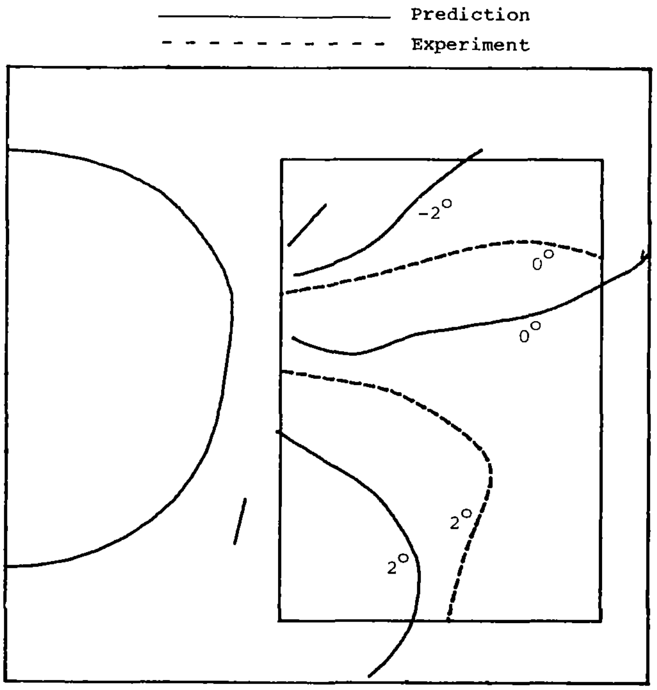

(b) β_l.

Figure 8.- Contours predicted from STEIN code and Tailor-Mate experimental data for side-mounted configuration at $M_\infty = 2.5$ and $\alpha = 5°$.

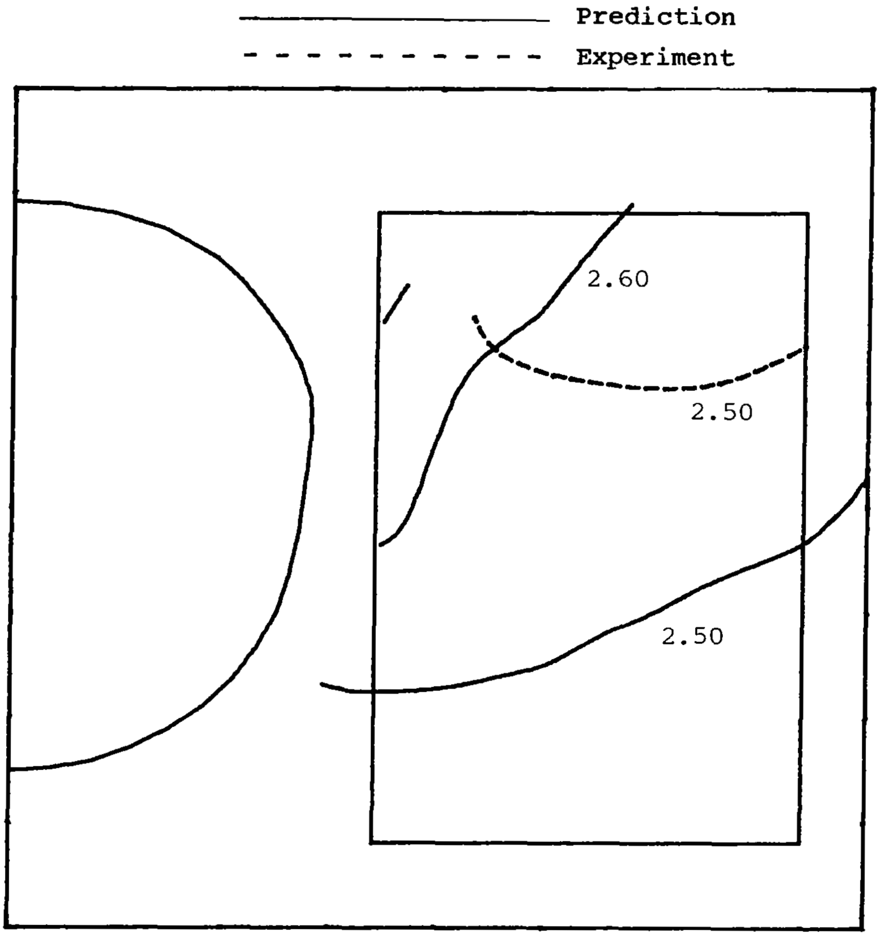

(c) M_l.

Figure 8.- Concluded.

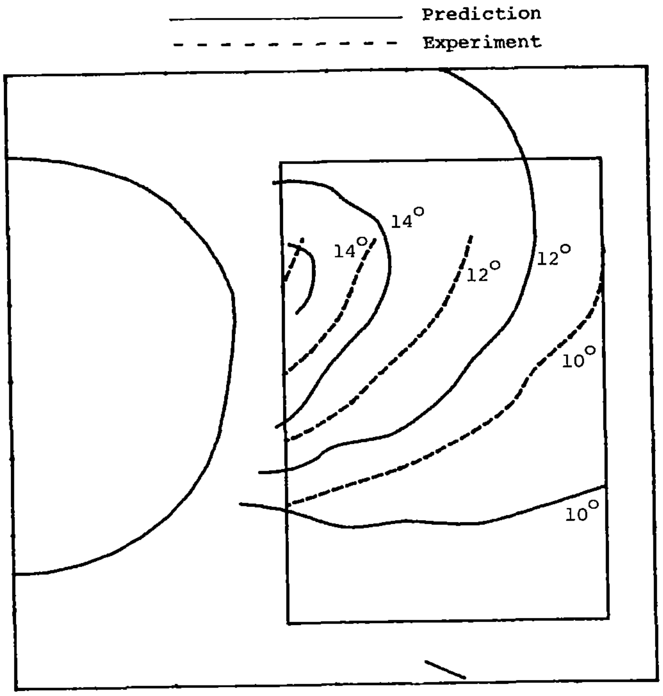

(a) α_l.

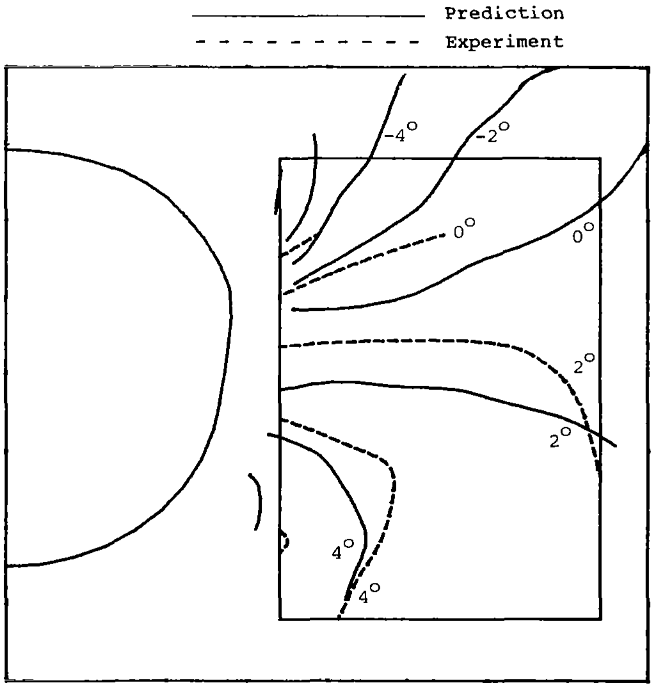

(b) β_l.

Figure 9.- Contours predicted from STEIN code and Tailor-Mate experimental data for side-mounted configuration at $M_\infty = 2.5$ and $\alpha = 10°$.

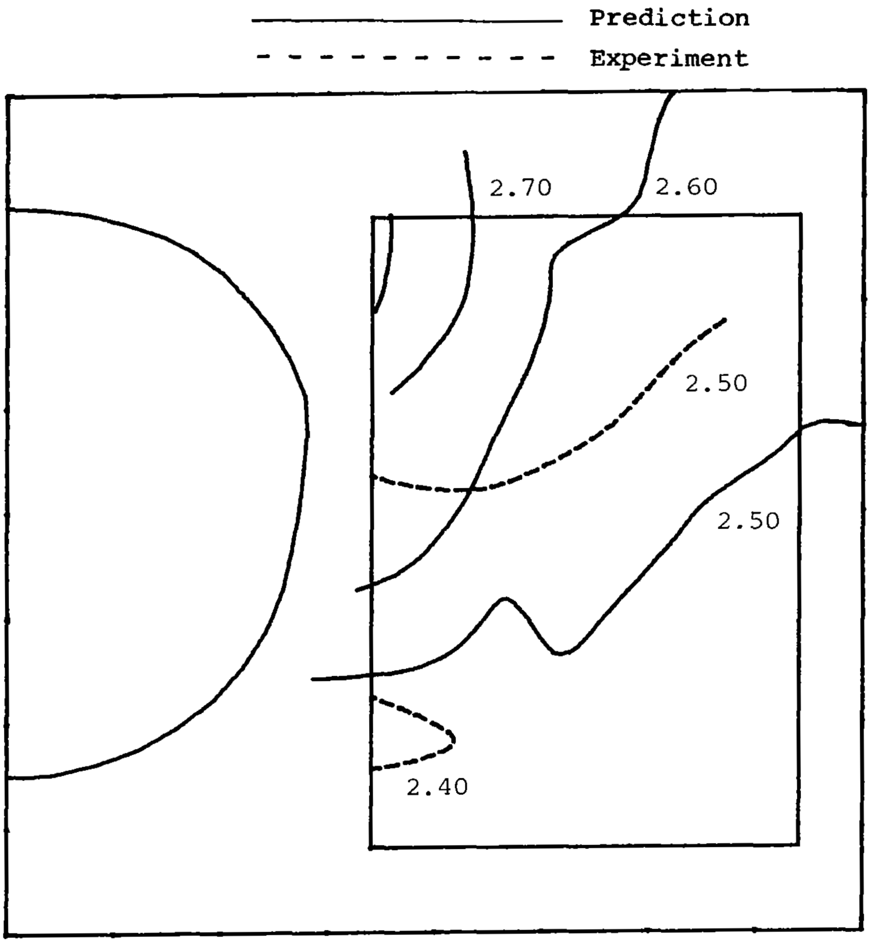

(c) M_l.

Figure 9.- Concluded.

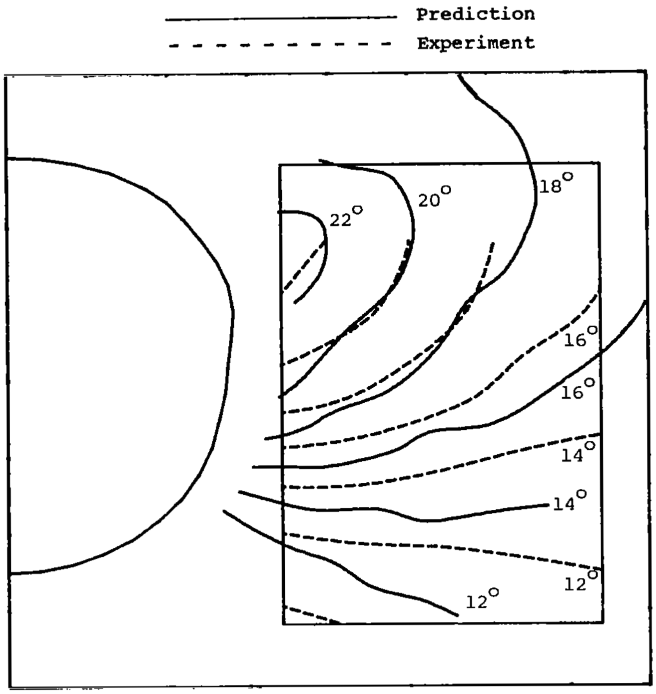

(a) α_l.

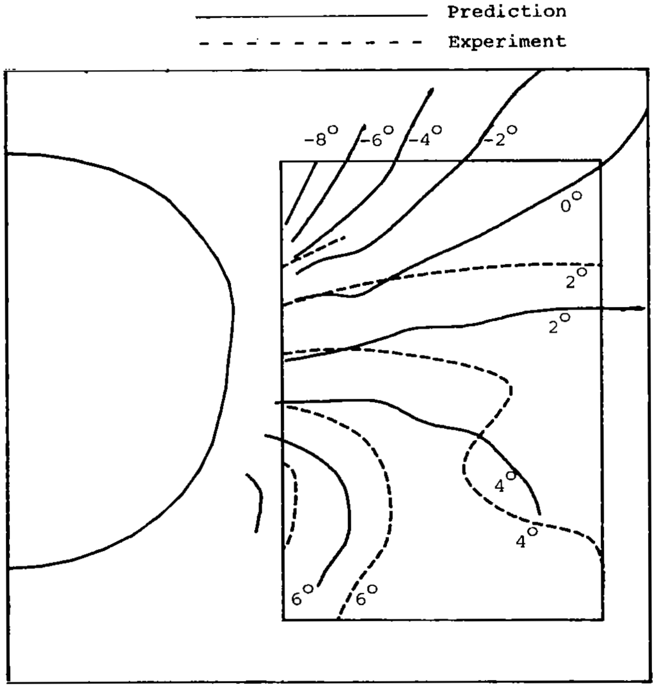

(b) β_l.

Figure 10.- Contours predicted from STEIN code and Tailor-Mate experimental data for side-mounted configuration at $M_\infty = 2.5$ and $\alpha = 15°$.

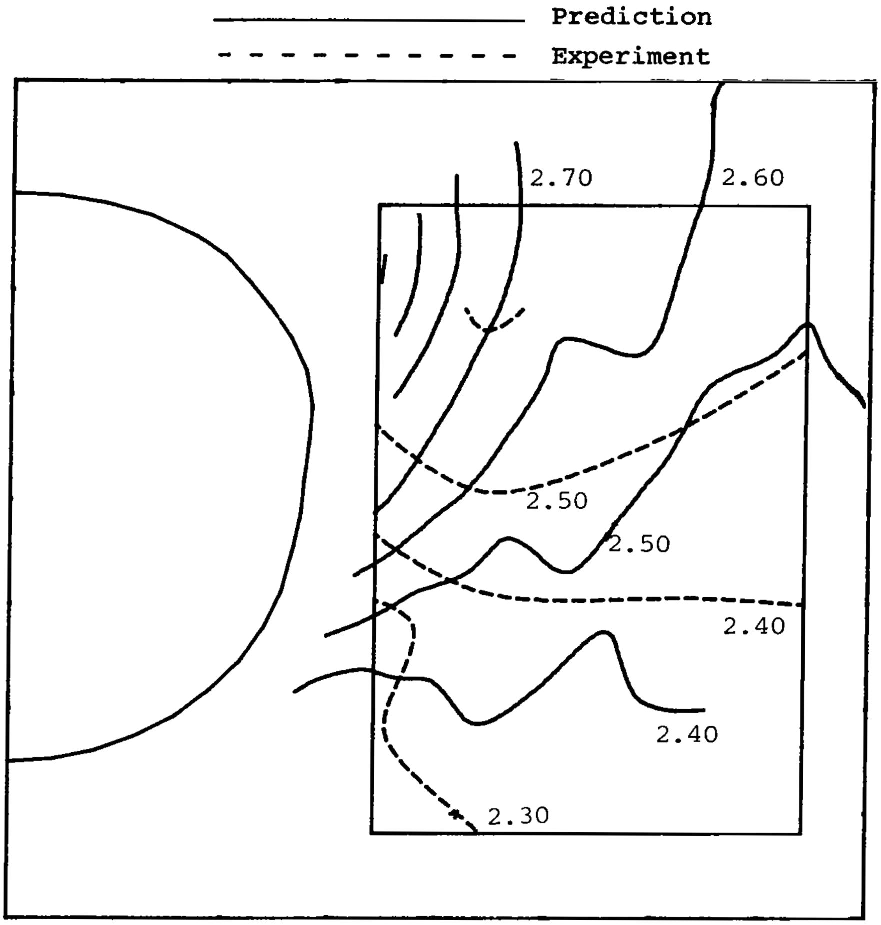

(c) M_l.

Figure 10.- Concluded.

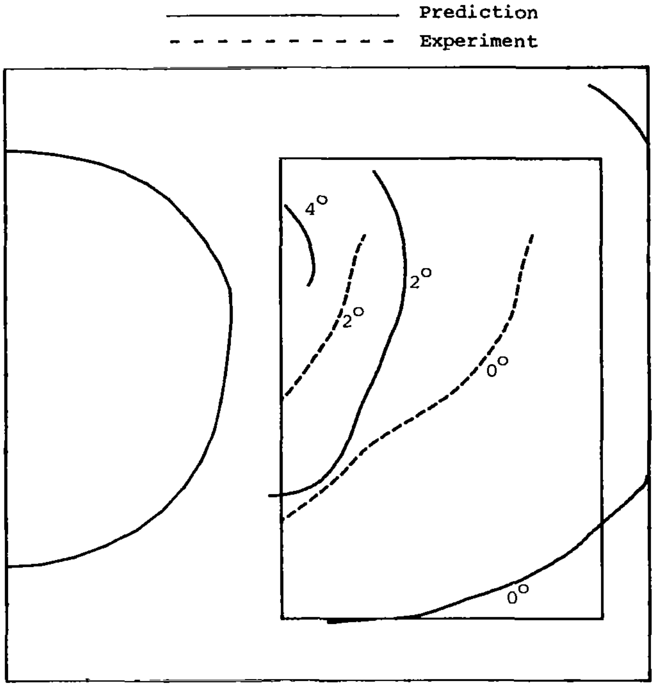

(a) α_l.

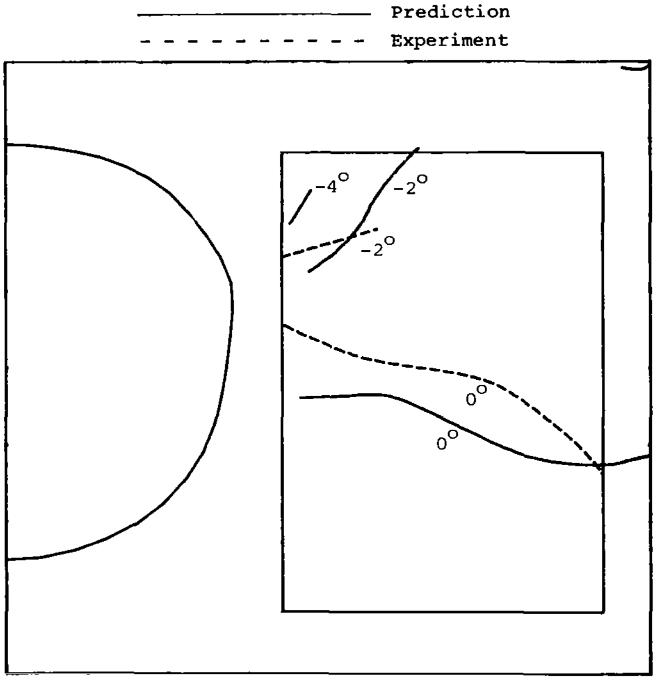

(b) β_l.

Figure 11.- Contours predicted from STEIN code and Tailor-Mate experimental data for side-mounted configuration at $M_\infty = 2.2$ and $\alpha = 0°$.

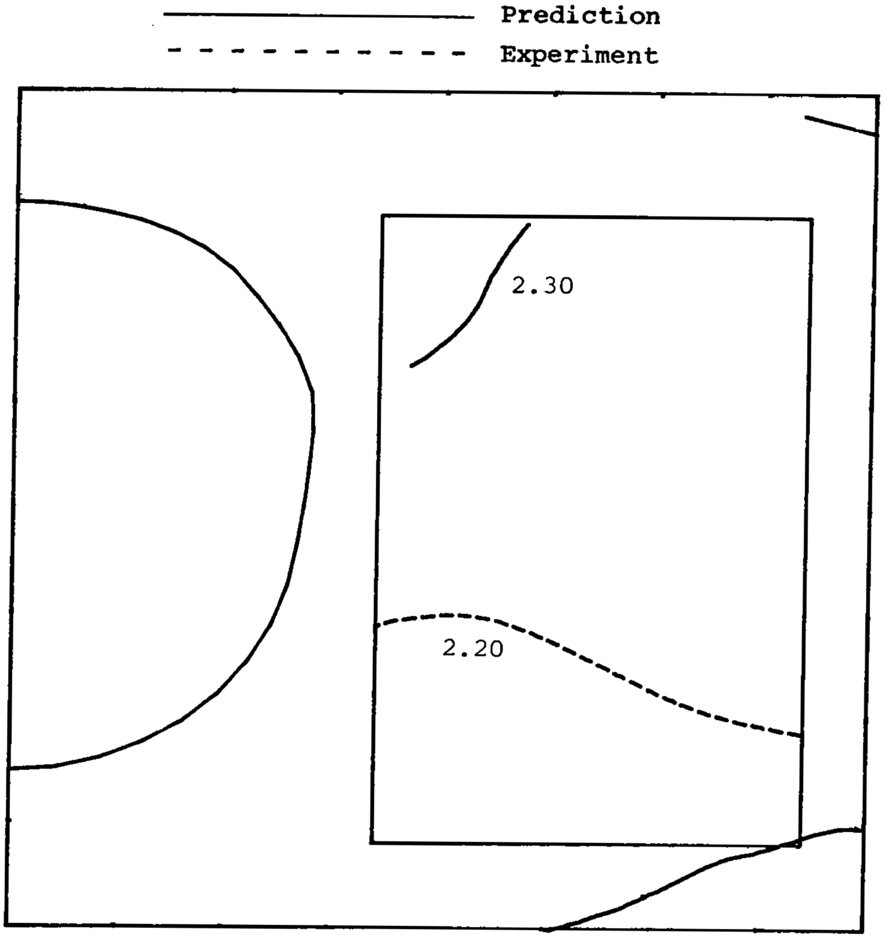

(c) M_l.

Figure 11.- Concluded.

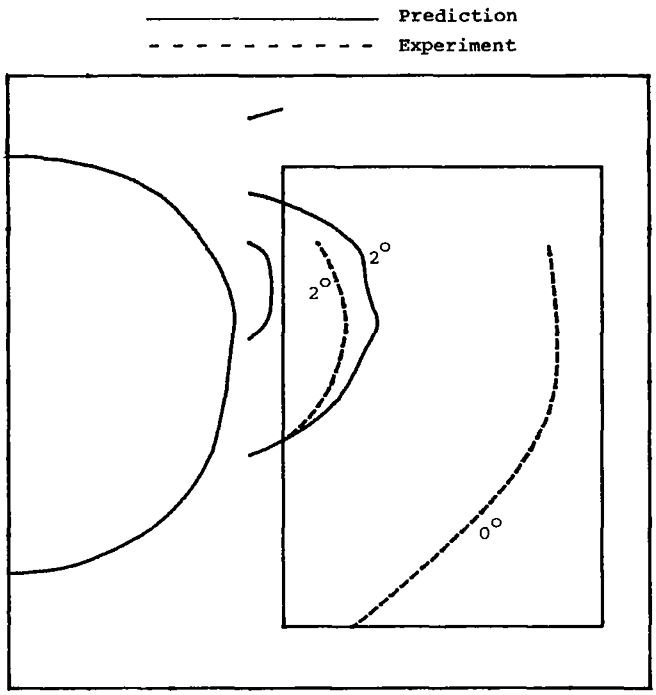

(a) α_l.

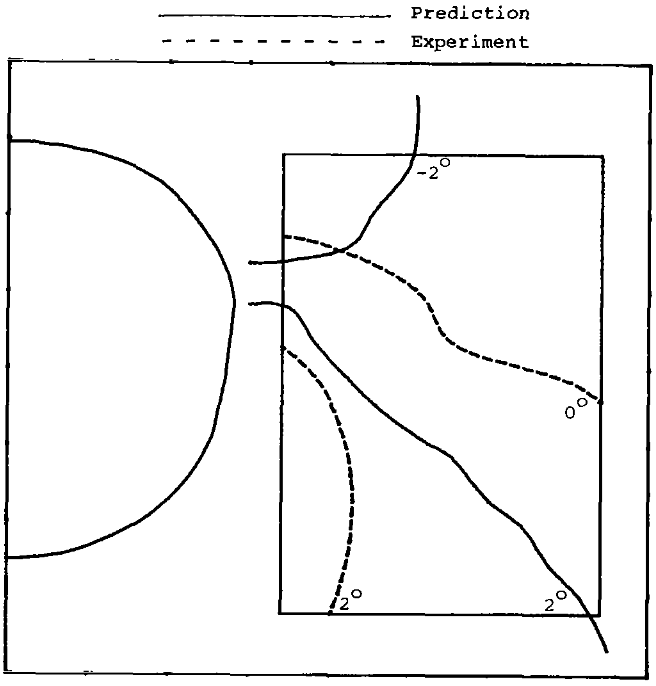

(b) β_l.

Figure 12.- Contours predicted from WIBCO code and Tailor-Mate experimental data for side-mounted configuration at $M_\infty = 0.9$ and $\alpha = 0°$.

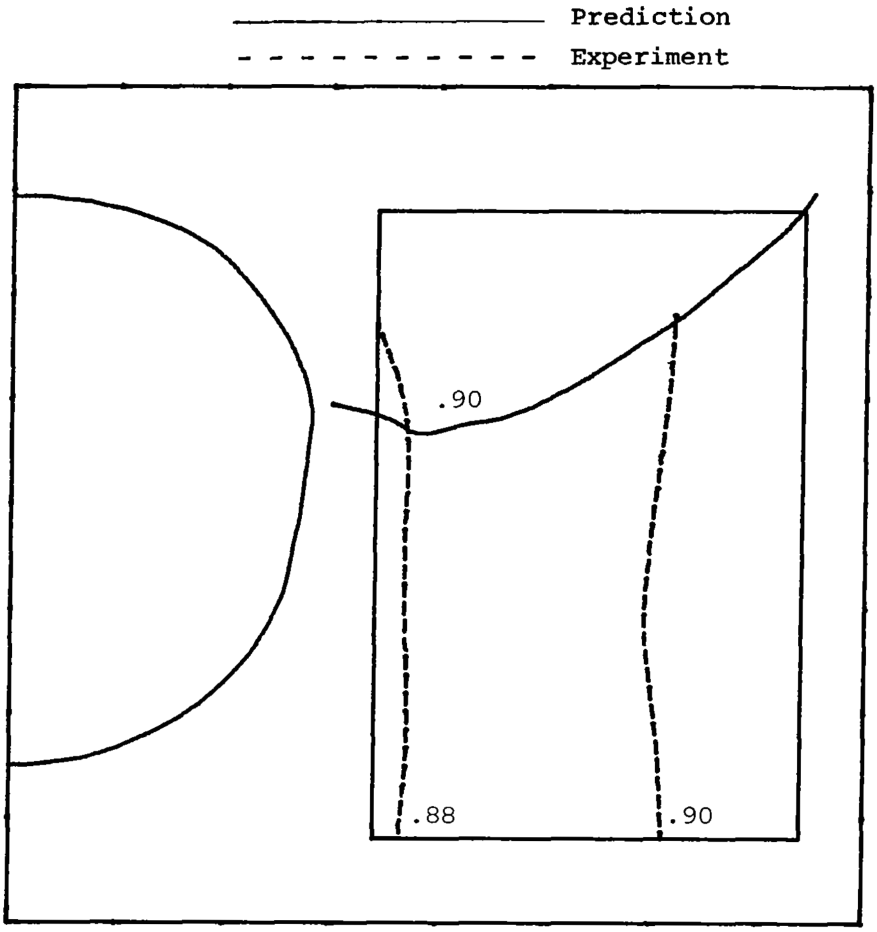

(c) M_l.

Figure 12.- Concluded.

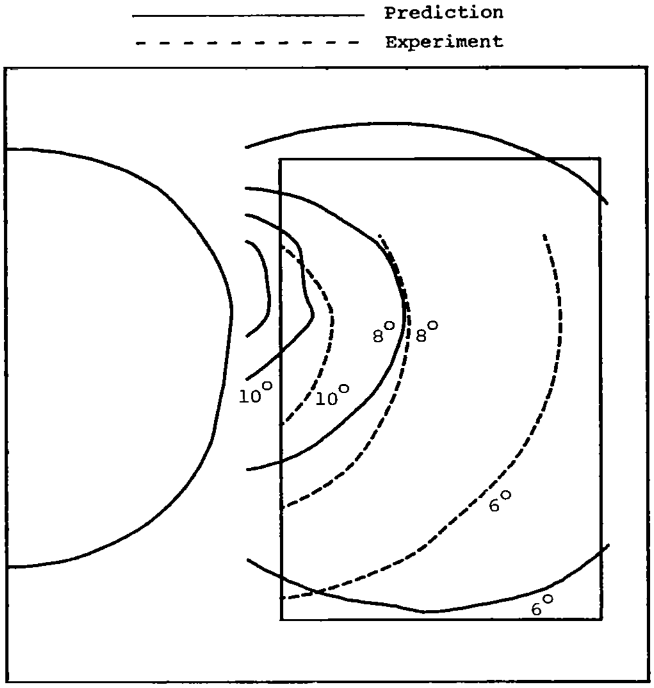

(a) α_l.

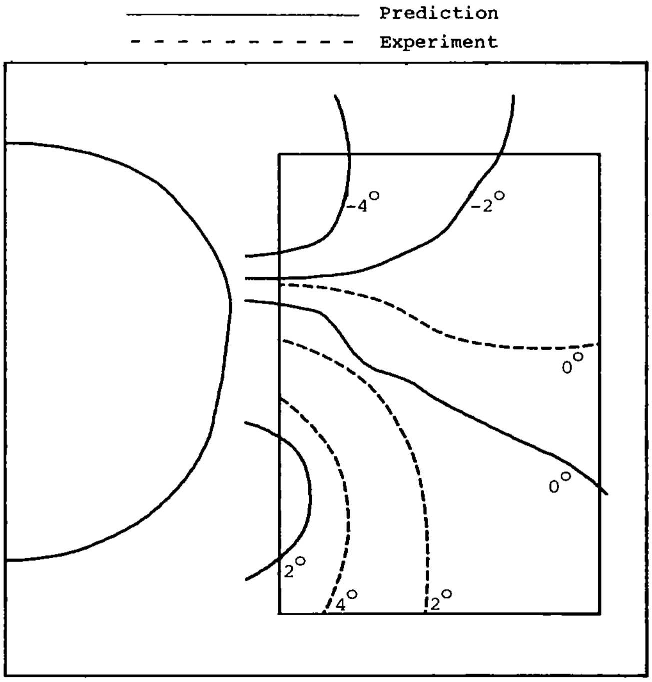

(b) β_l.

Figure 13.- Contours predicted from WIBCO code and Tailor-Mate experimental data for side-mounted configuration at $M_\infty = 0.9$ and $\alpha = 5°$.

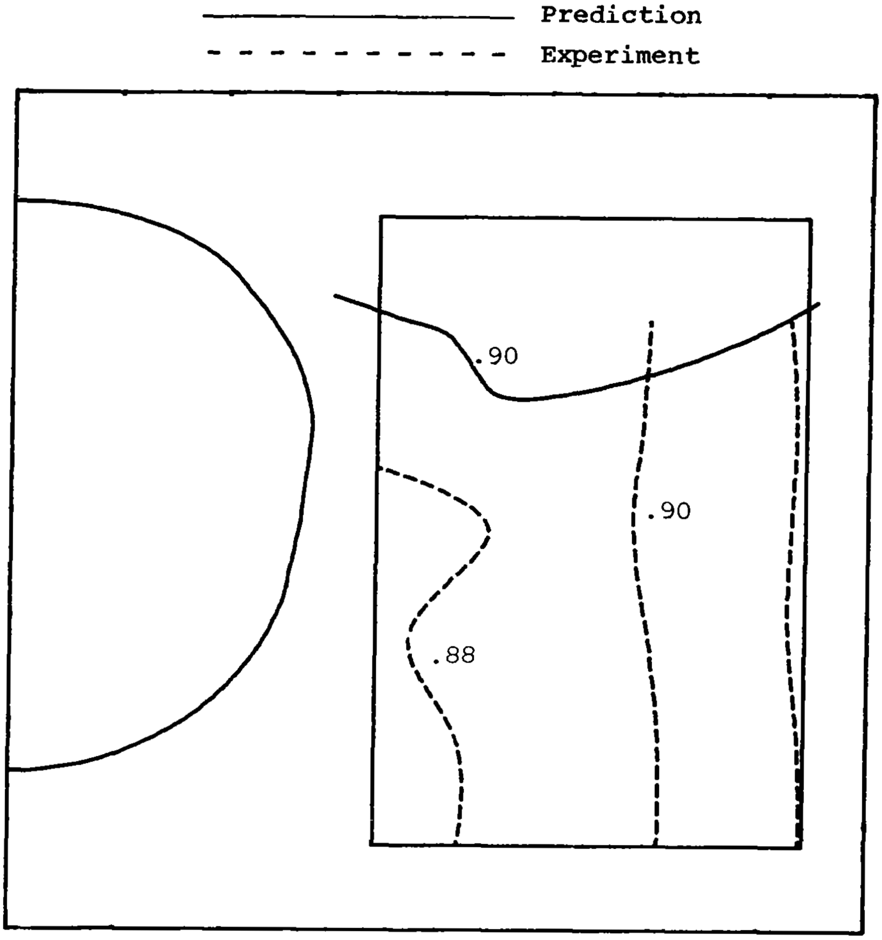

(c) M_l.

Figure 13.- Concluded.

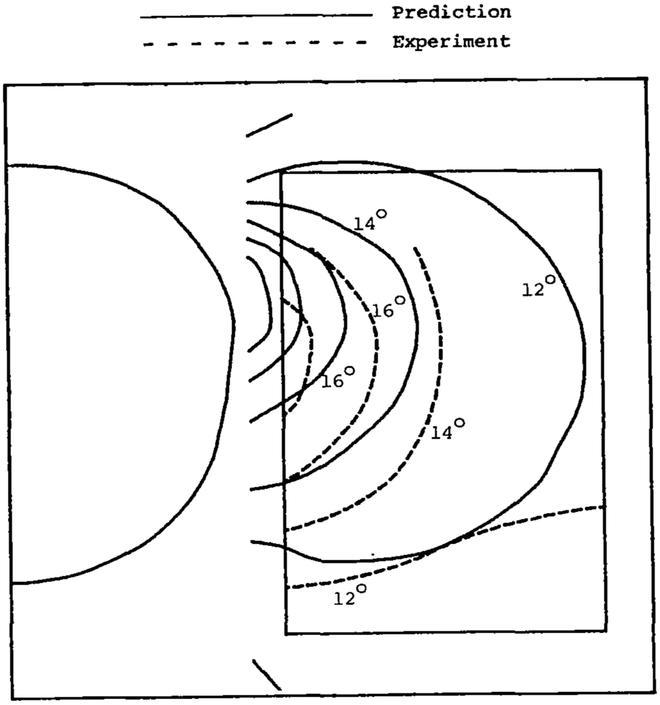

(a) α_l.

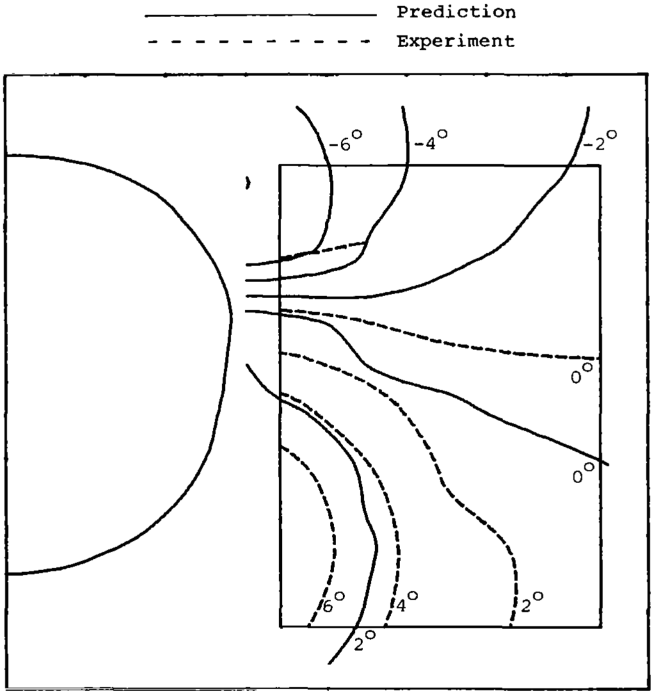

(b) β_l.

Figure 14.- Contours predicted from WIBCO code and Tailor-Mate experimental data for side-mounted configuration at $M_\infty = 0.9$ and $\alpha = 10°$.

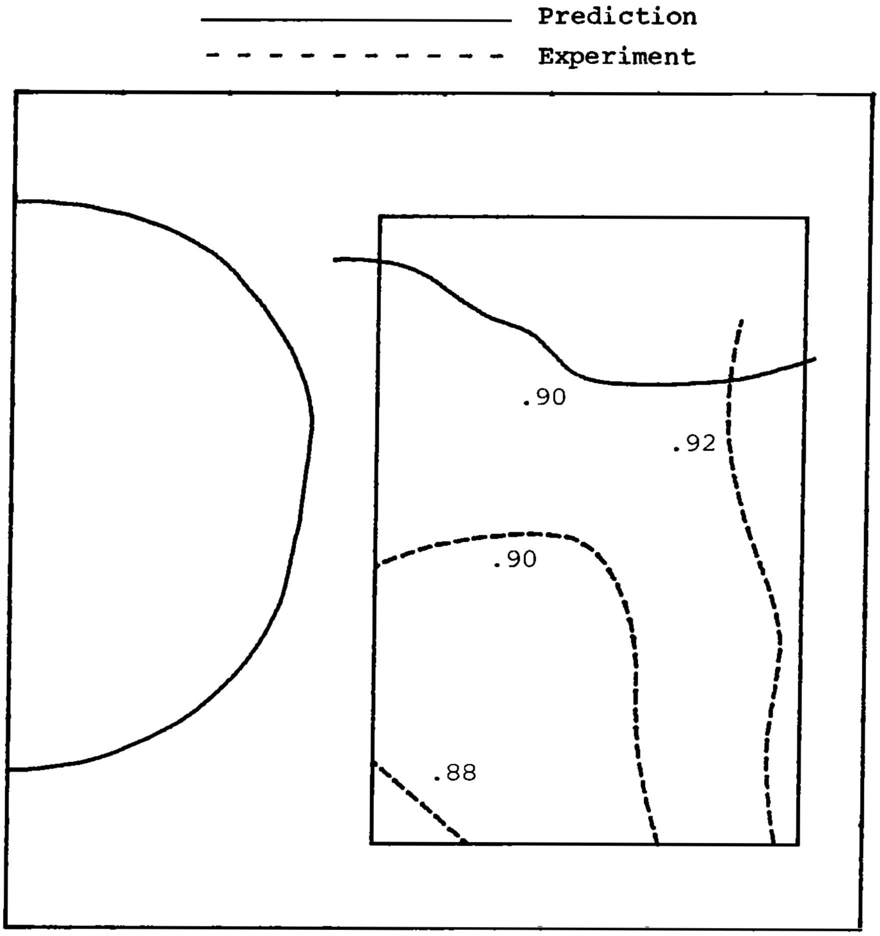

(c) M_l.

Figure 14.- Concluded.

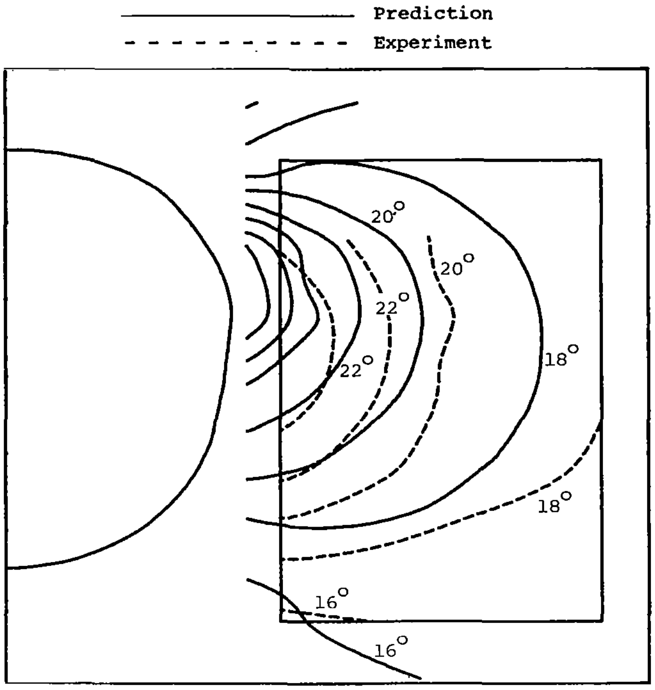

(a) α_l.

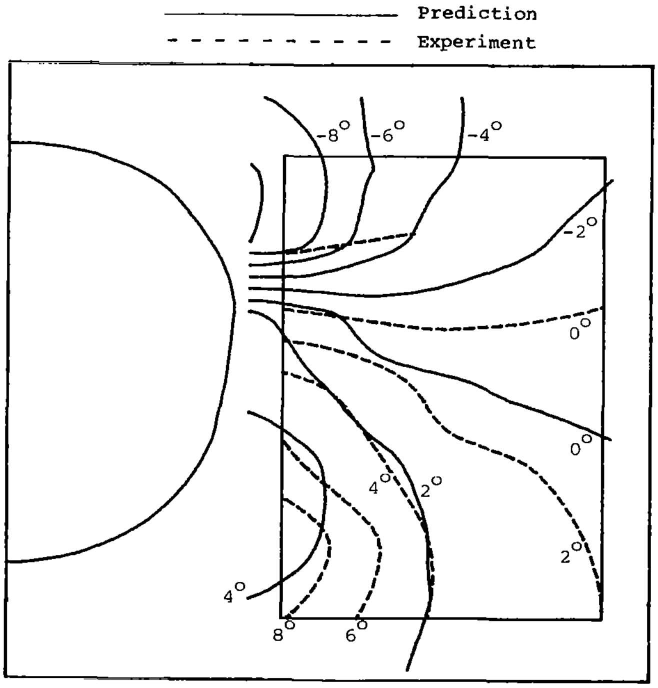

(b) β_l.

Figure 15.- Contours predicted from WIBCO code and Tailor-Mate experimental data for side-mounted configuration at $M_\infty = 0.9$ and $\alpha = 15°$.

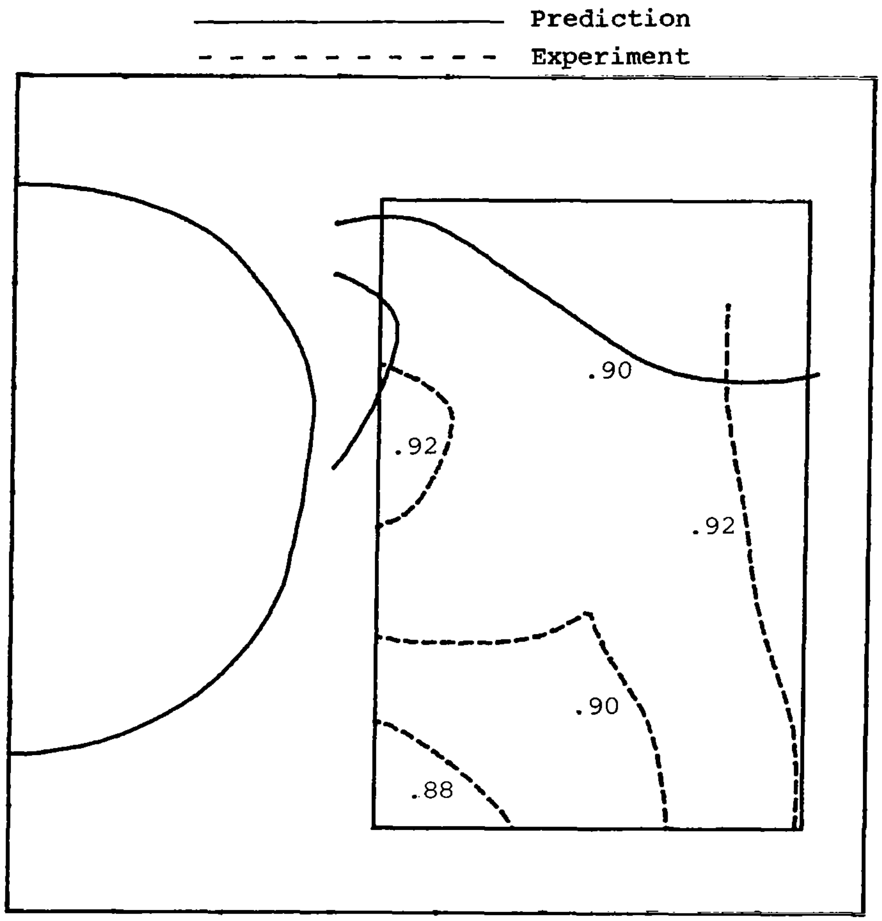

(c) M_l.

Figure 15.- Concluded.

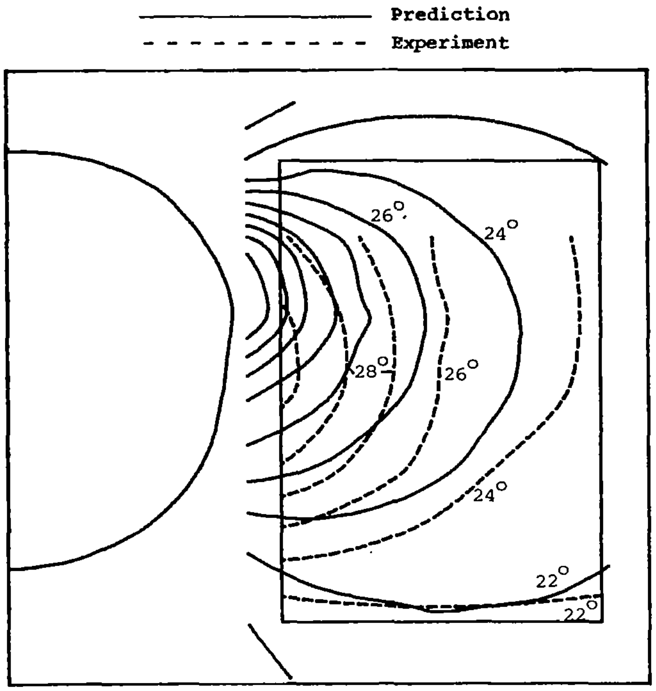

(a) α_l.

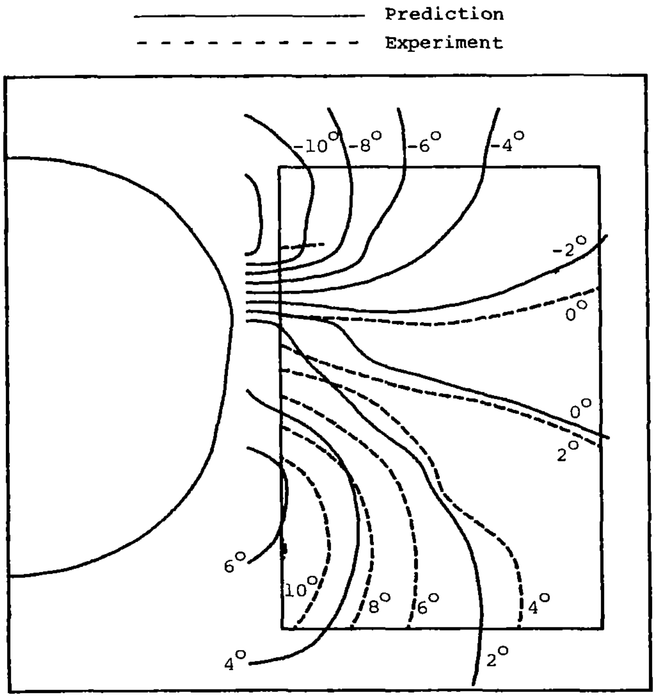

(b) β_l.

Figure 16.- Contours predicted from WIBCO code and Tailor-Mate experimental data for side-mounted configuration at $M_\infty = 0.9$ and $\alpha = 20°$.

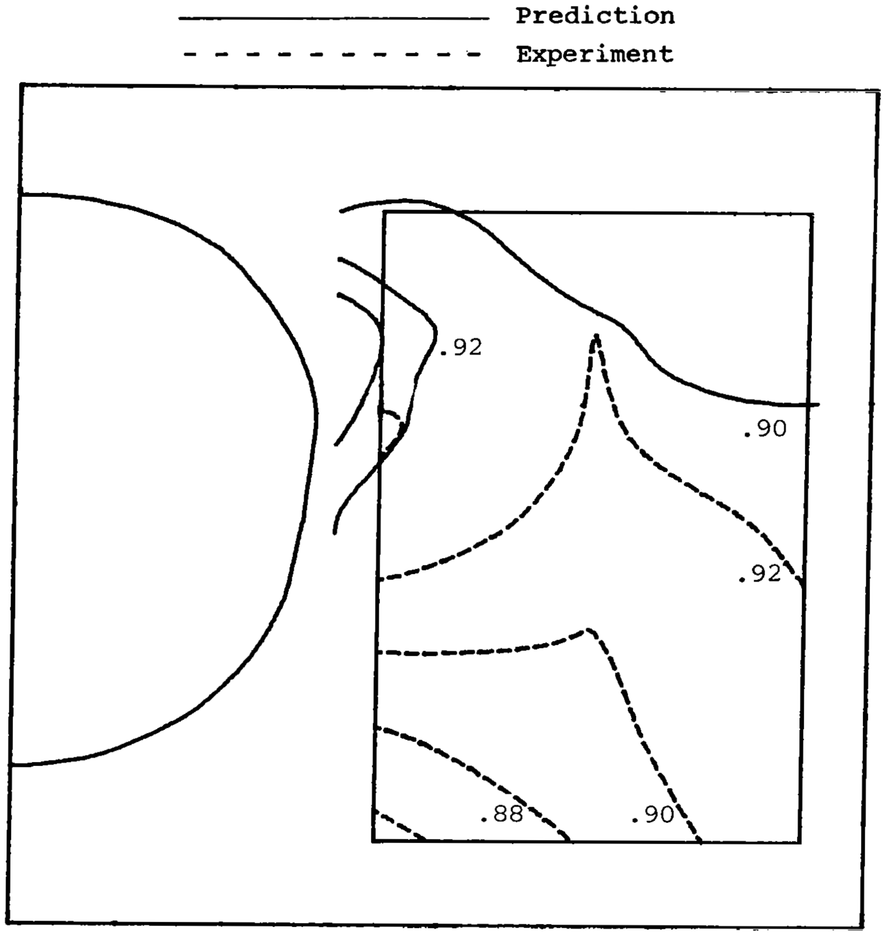

(c) M_l.

Figure 16.- Concluded.

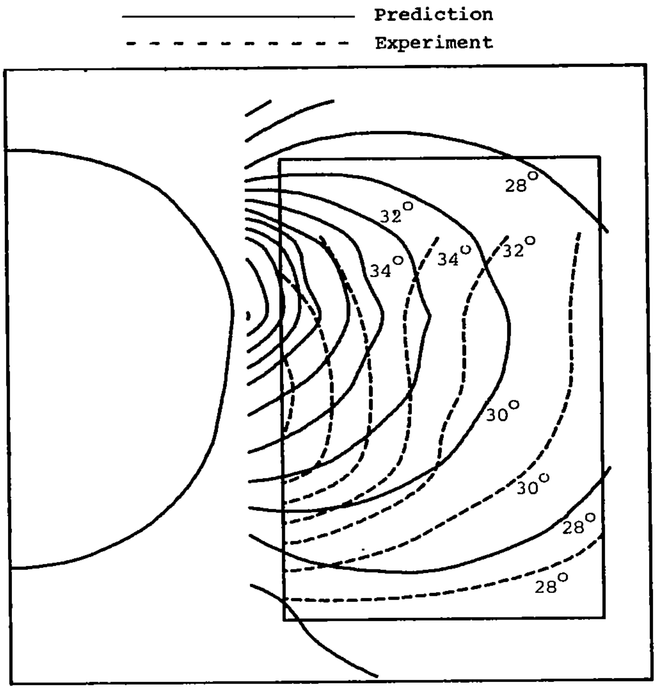

(a) α_l.

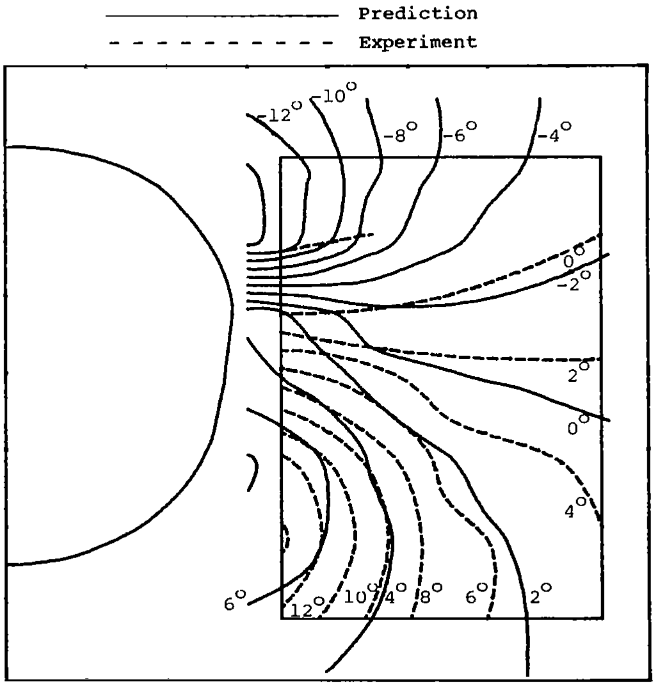

(b) β_l.

Figure 17.- Contours predicted from WIBCO code and Tailor-Mate experimental data for side-mounted configuration at $M_\infty = 0.9$ and $\alpha = 25°$.

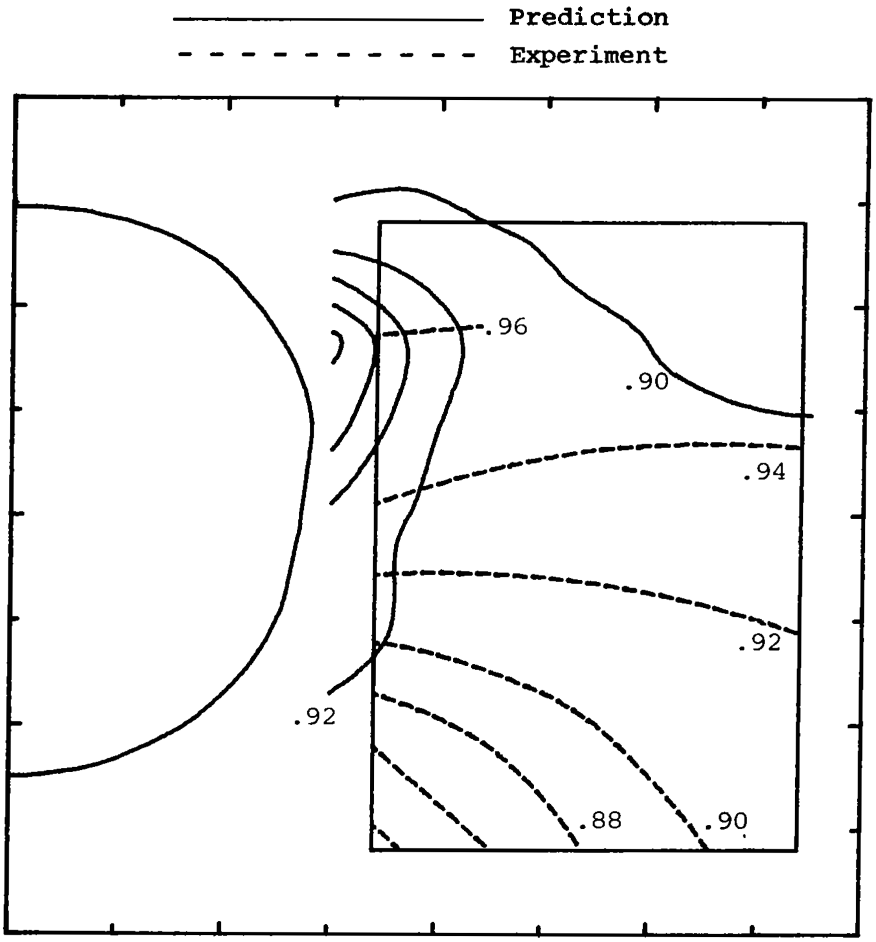

(c) M_l.

Figure 17.- Concluded.

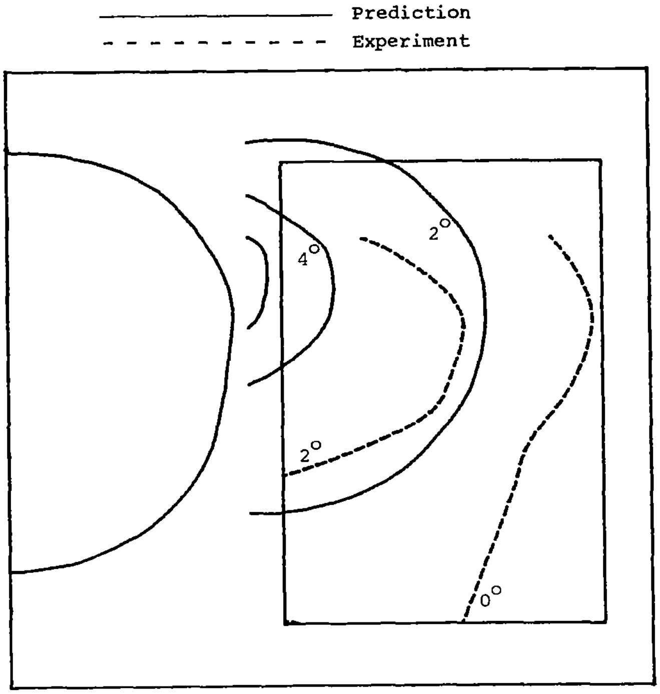

(a) α_l.

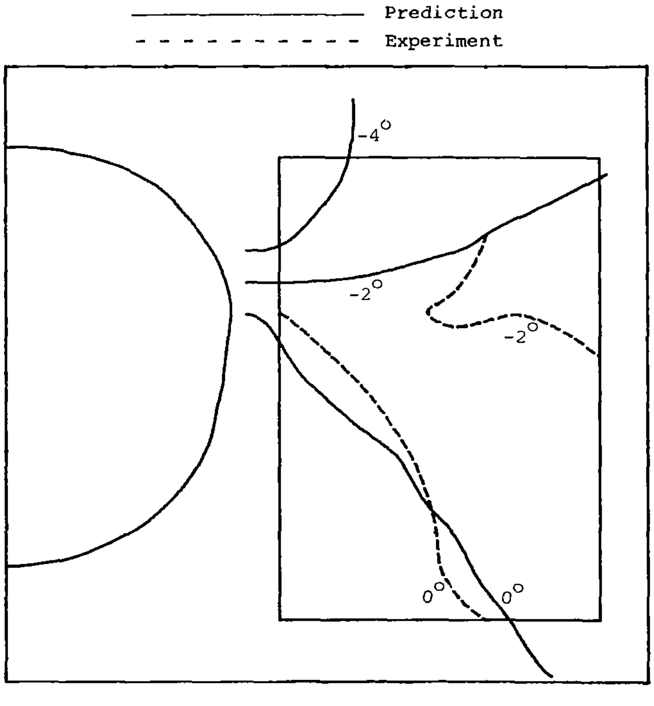

(b) β_l.

Figure 18.- Contours predicted from WIBCO code and Tailor-Mate experimental data for side-mounted configuration at $M_\infty = 1.6$ and $\alpha = 0°$.

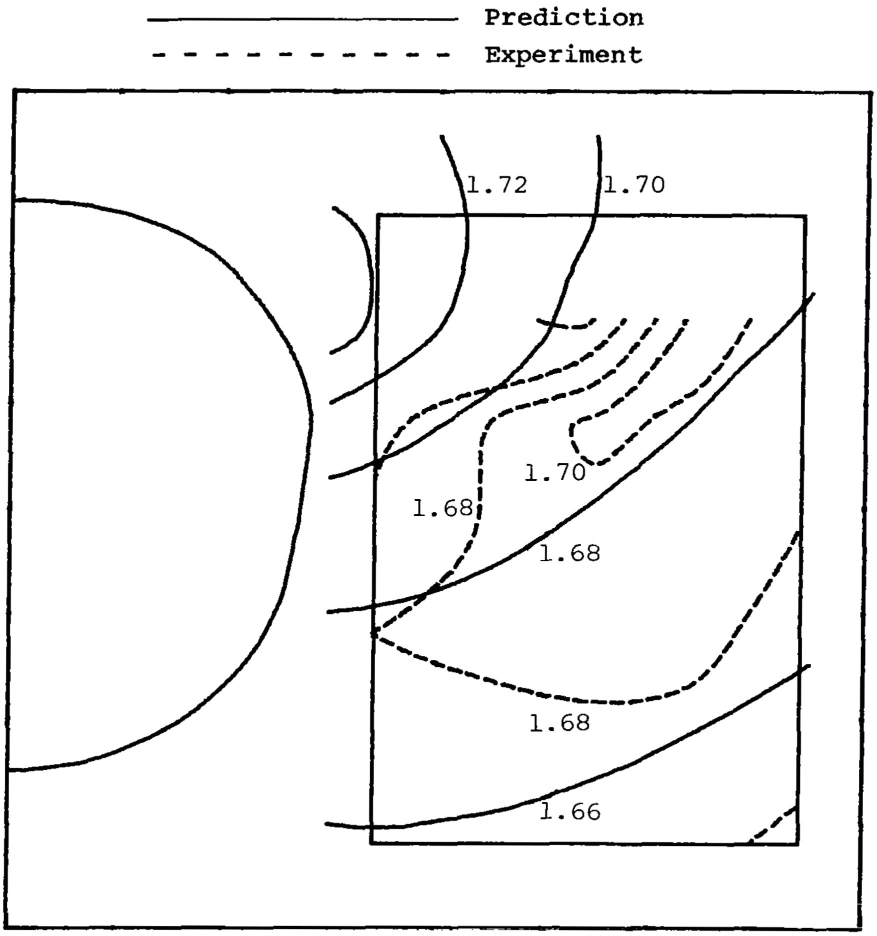

(c) M_l.

Figure 18.- Concluded.

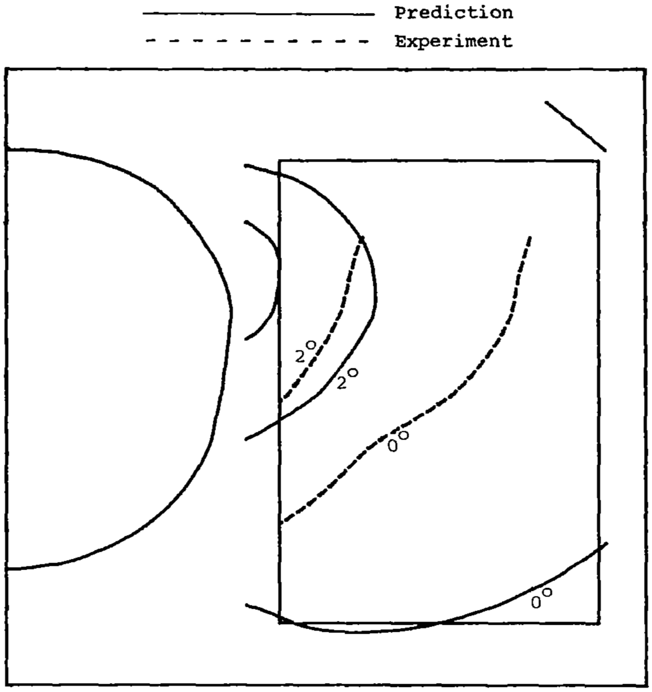

(a) α_l.

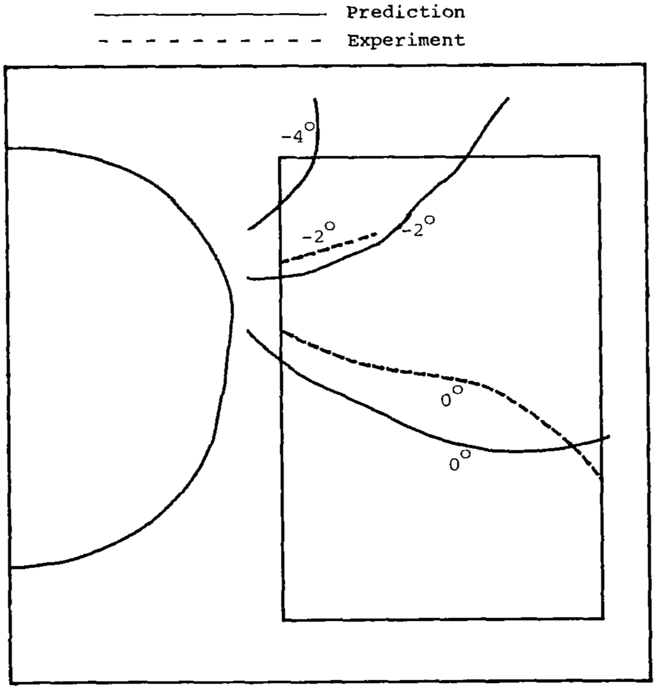

(b) β_l.

Figure 19.- Contours predicted from WIBCO code and Tailor-Mate experimental data for side-mounted configuration at $M_\infty = 2.2$ and $\alpha = 0°$.

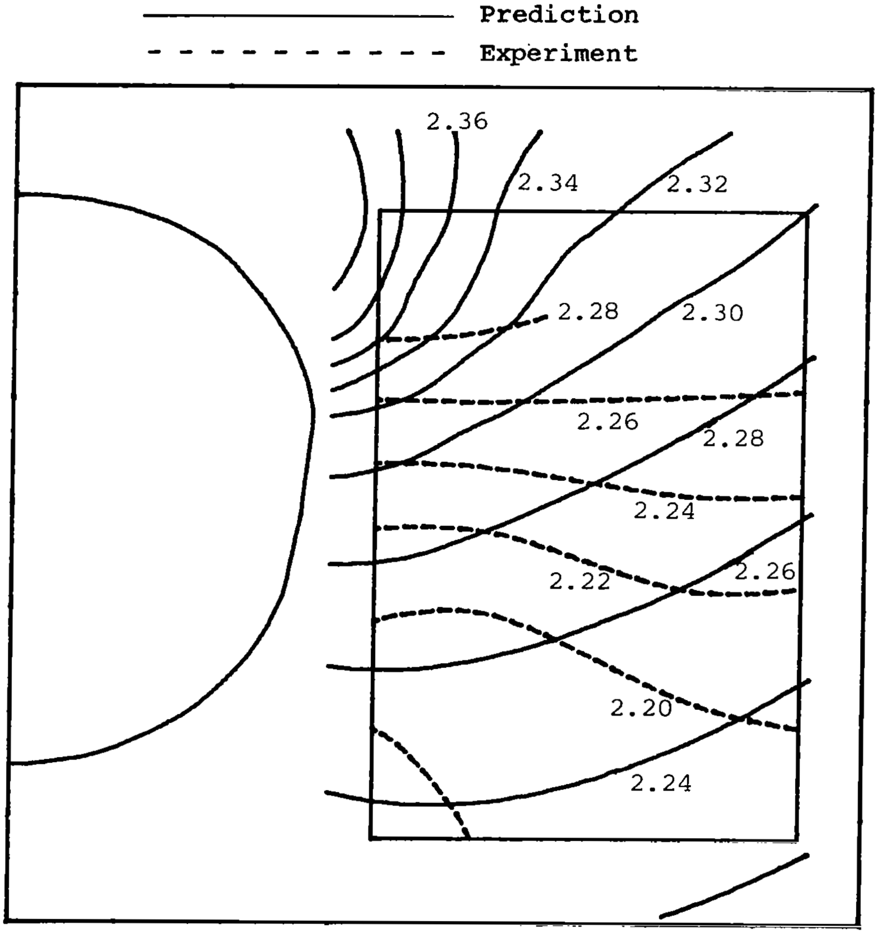

(c) M_l.

Figure 19.- Concluded.

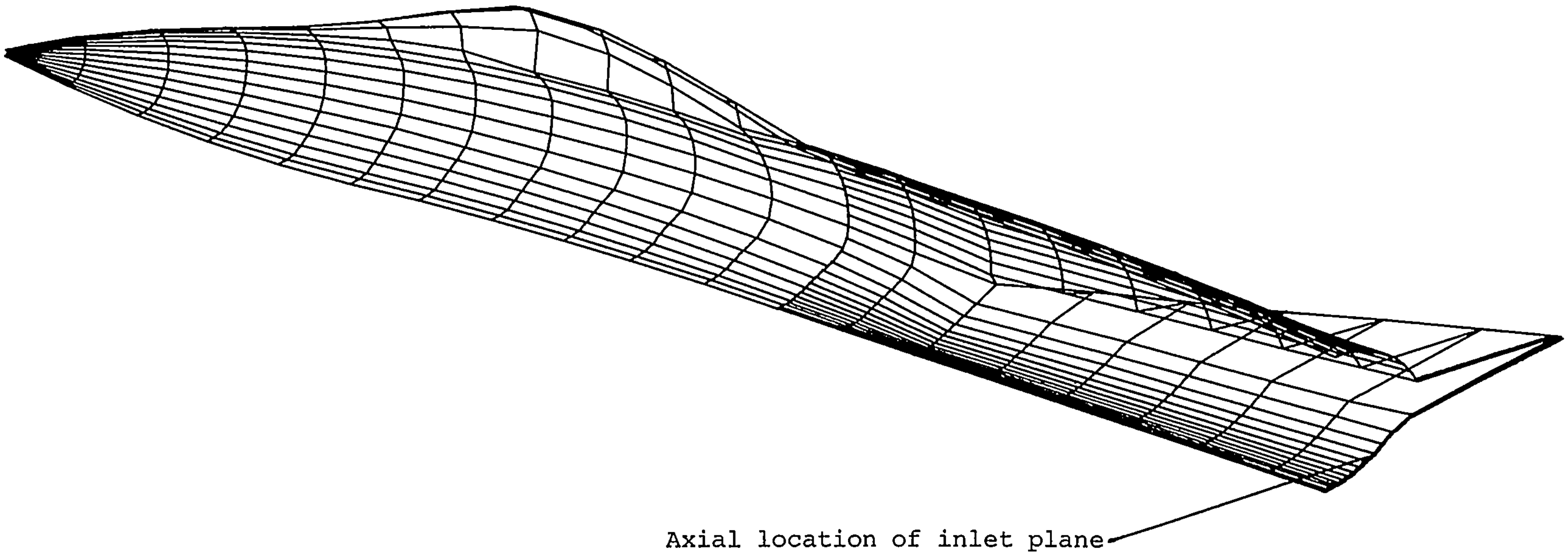

Figure 20.- QUICK-geometry model of Tailor-Mate wing-shielded inlet configuration for use with STEIN code.

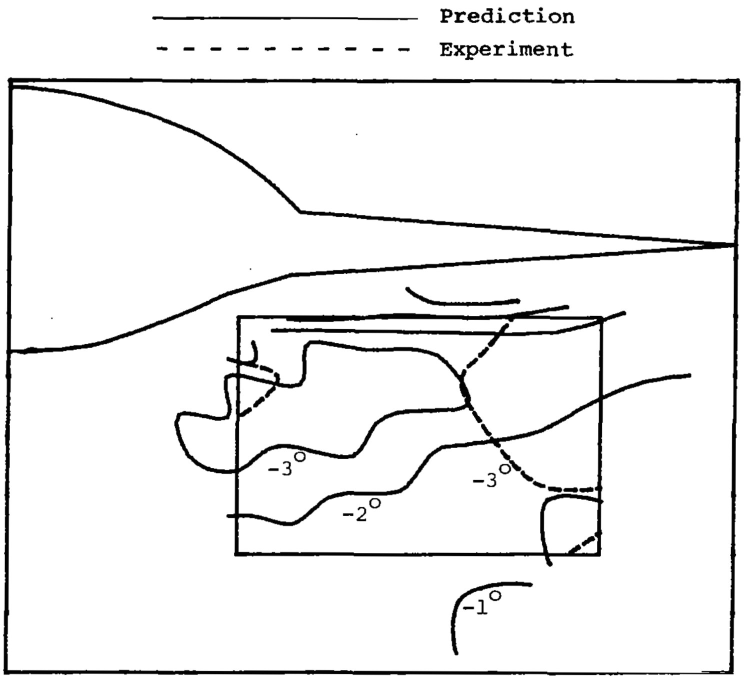

(a) α_l.

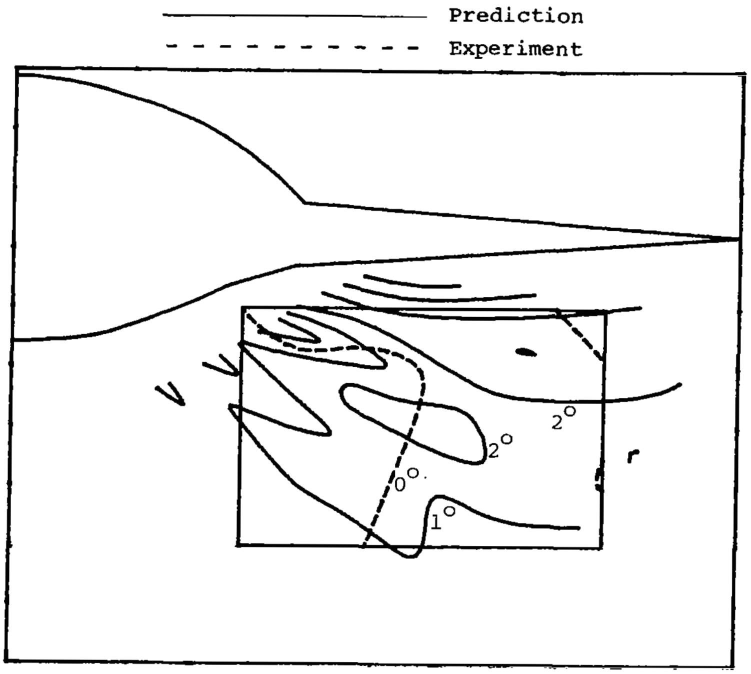

(b) β_l.

Figure 21.- Contours predicted from STEIN code and Tailor-Mate experimental data for wing-shielded configuration at $M_\infty = 2.5$ and $\alpha = 0°$.

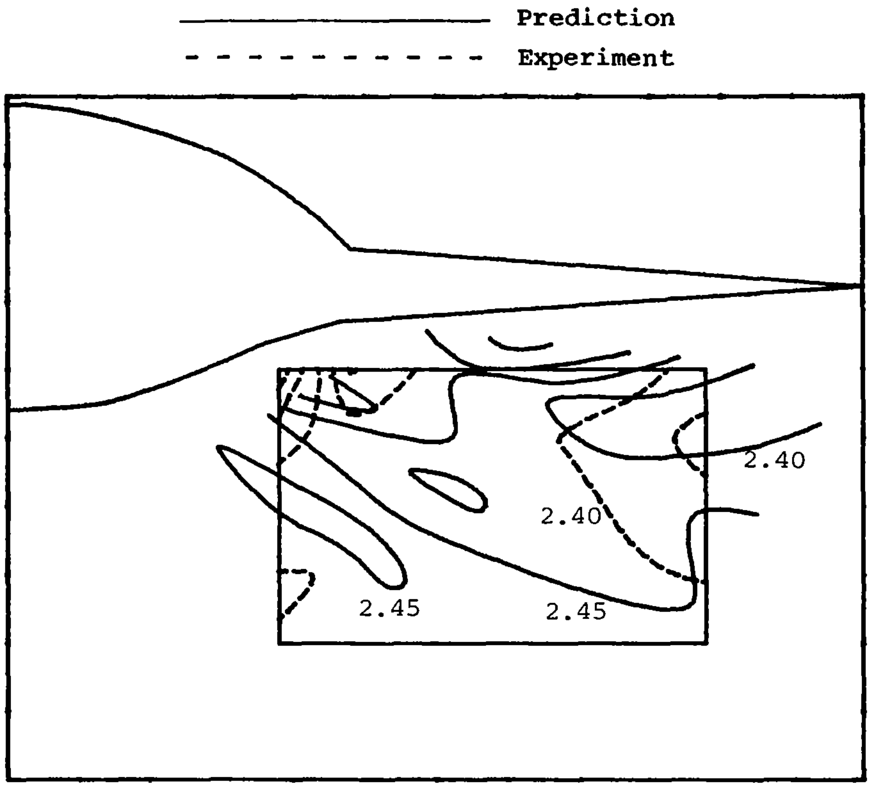

(c) M_l.

Figure 21.- Concluded.

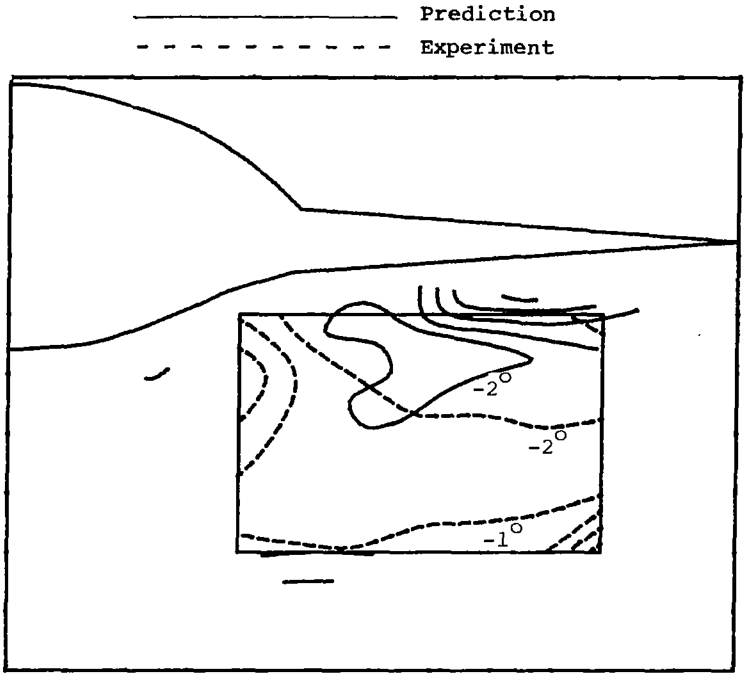

(a) α_l.

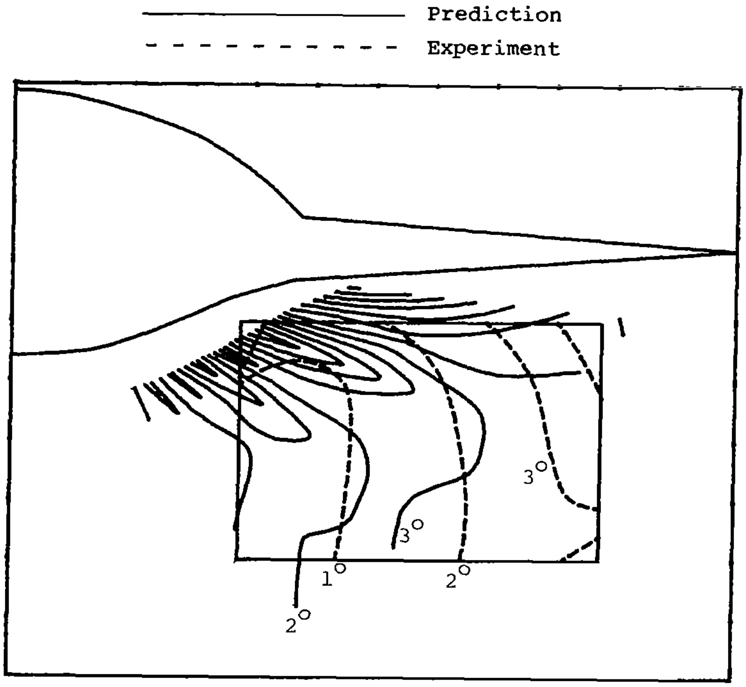

(b) β_l.

Figure 22.- Contours predicted from STEIN code and Tailor-Mate experimental data for wing-shielded configuration at $M_\infty = 2.5$ and $\alpha = 5°$.

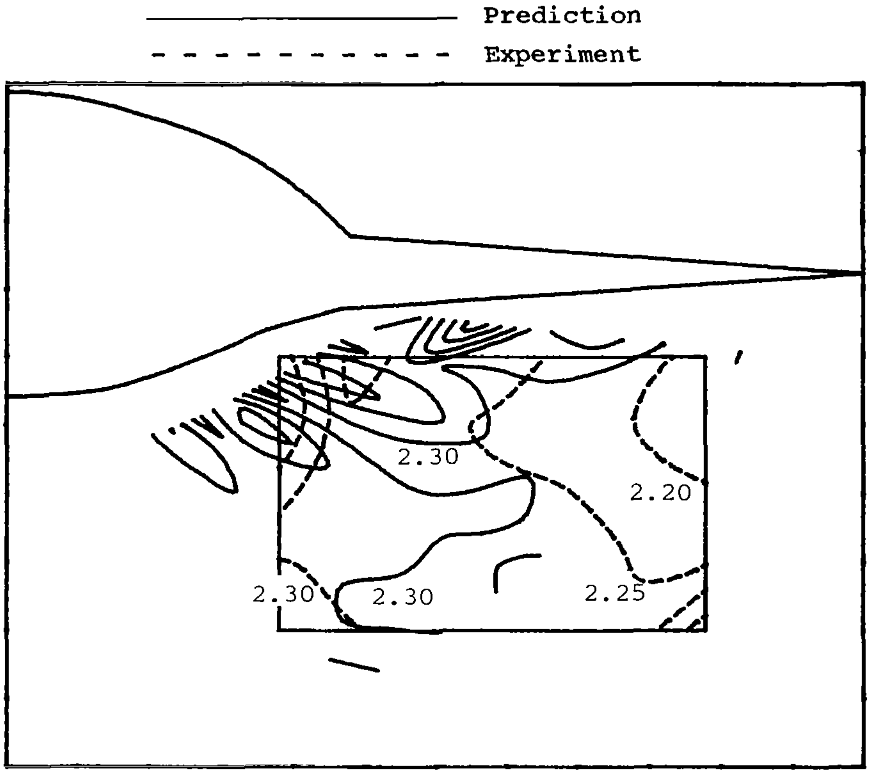

(c) M_l.

Figure 22.- Concluded.

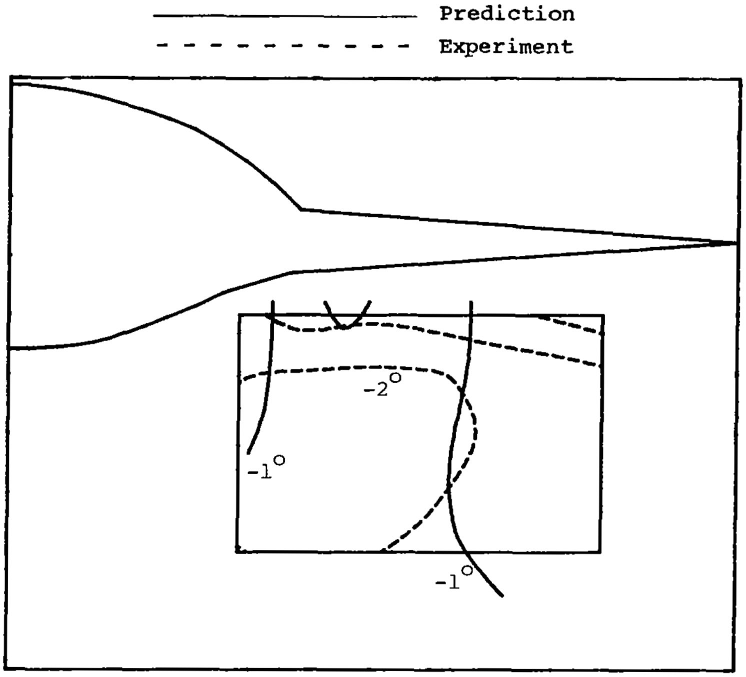

(a) α_l.

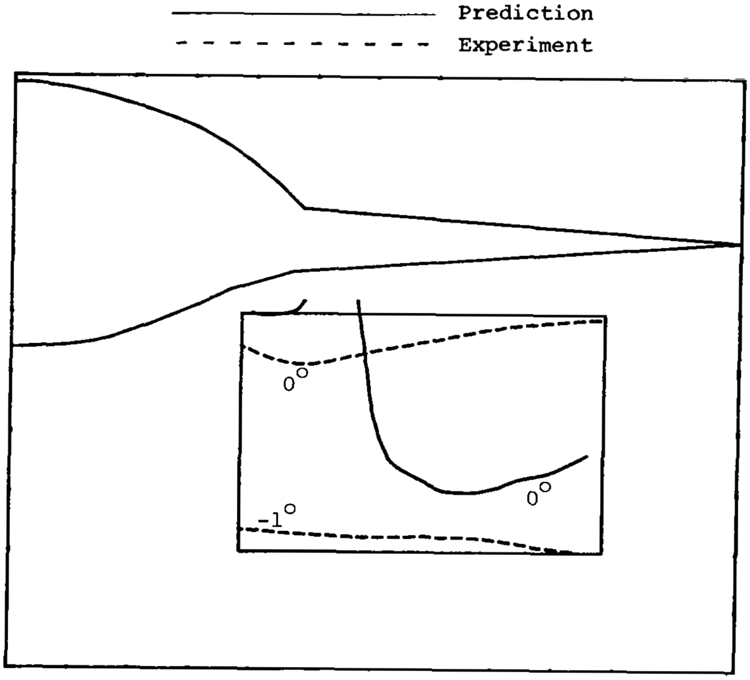

(b) β_l.

Figure 23.- Contours predicted from WIBCO code and Tailor-Mate experimental data for wing-shielded configuration at $M_\infty = 0.9$ and $\alpha = 0°$.

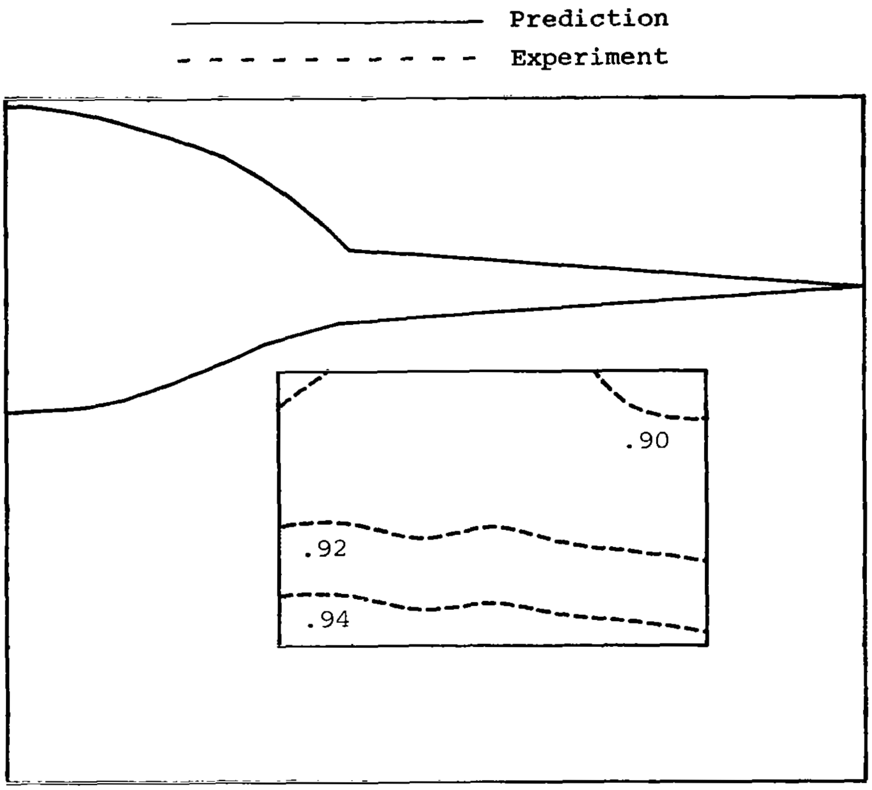

(c) M_l; all predicted data were between $M_l = 0.90$ and 0.92.

Figure 23.- Concluded.

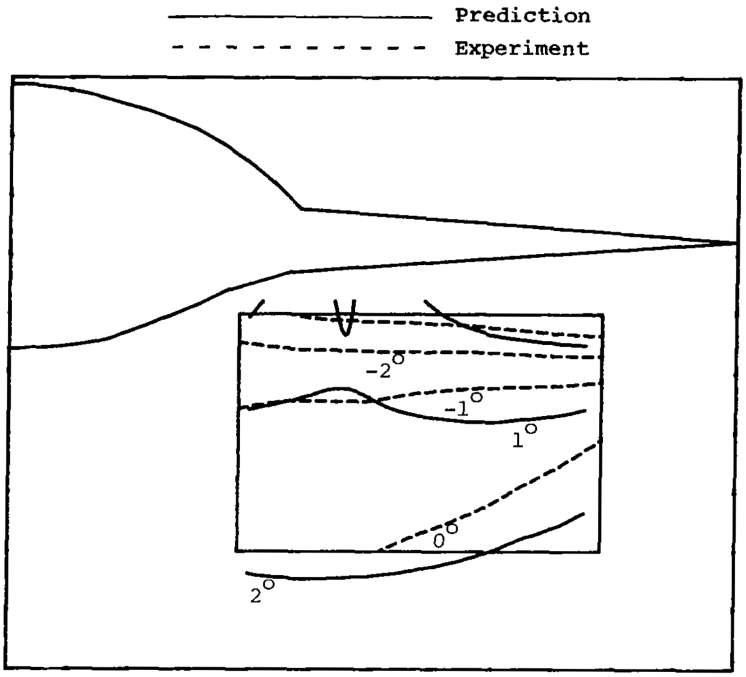

(a) α_l.

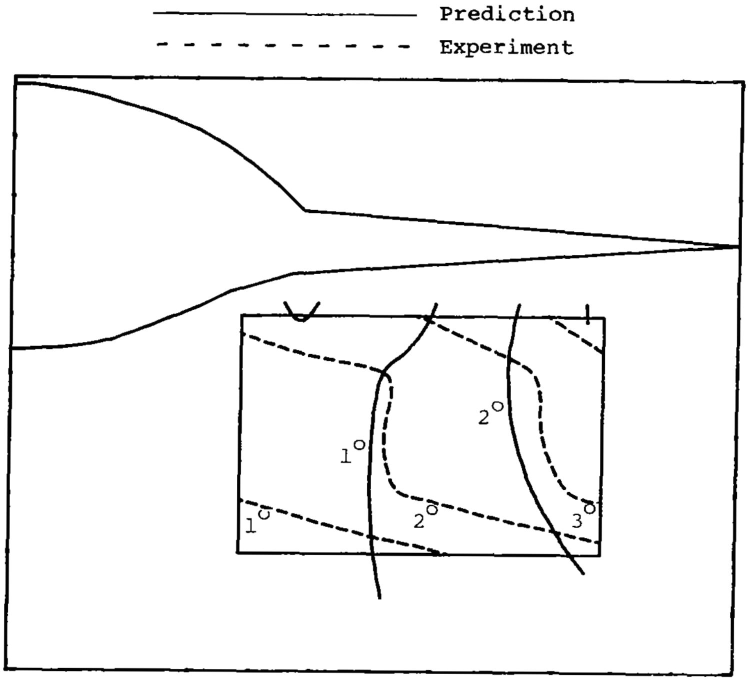

(b) β_l.

Figure 24.- Contours predicted from WIBCO code and Tailor-Mate experimental data for wing-shielded configuration at $M_\infty = 0.9$ and $\alpha = 5°$.

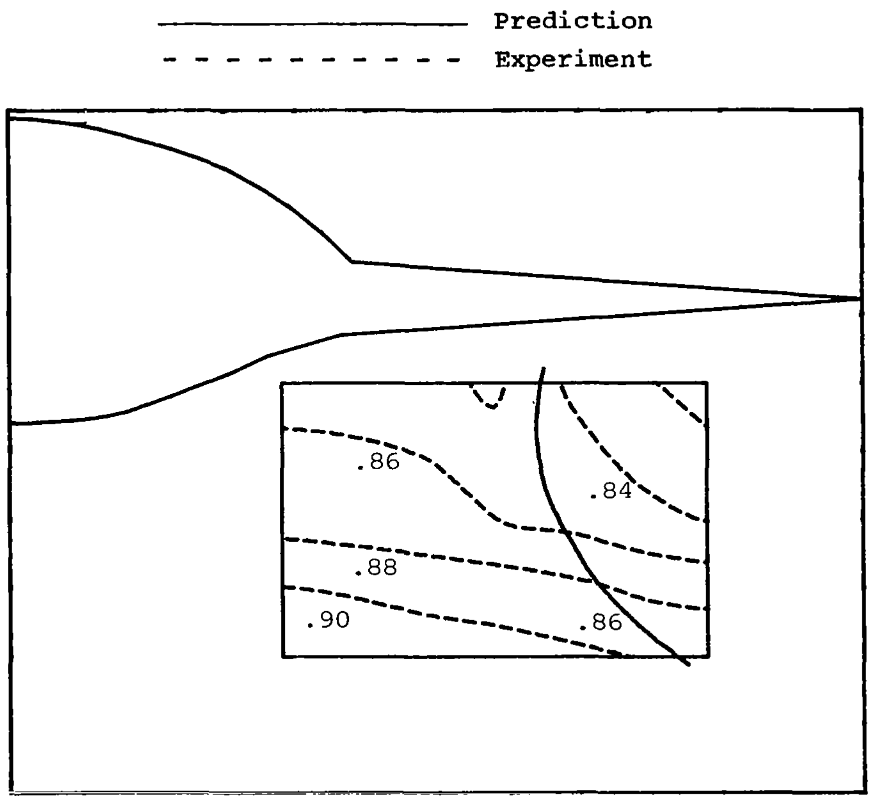

(c) M_l.

Figure 24.- Concluded.

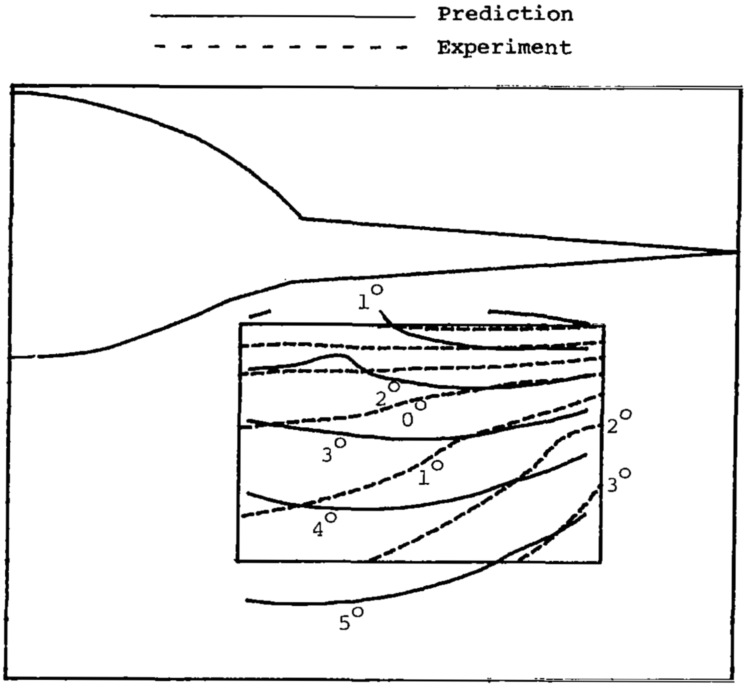

(a) α_l.

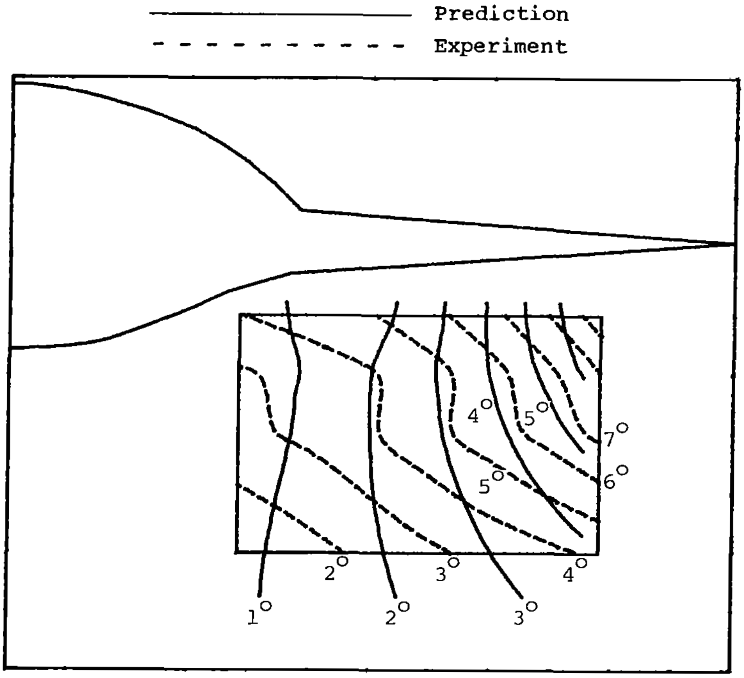

(b) β_l.

Figure 25.- Contours predicted from WIBCO code and Tailor-Mate experimental data for wing-shielded configuration at $M_\infty = 0.9$ and $\alpha = 10°$.

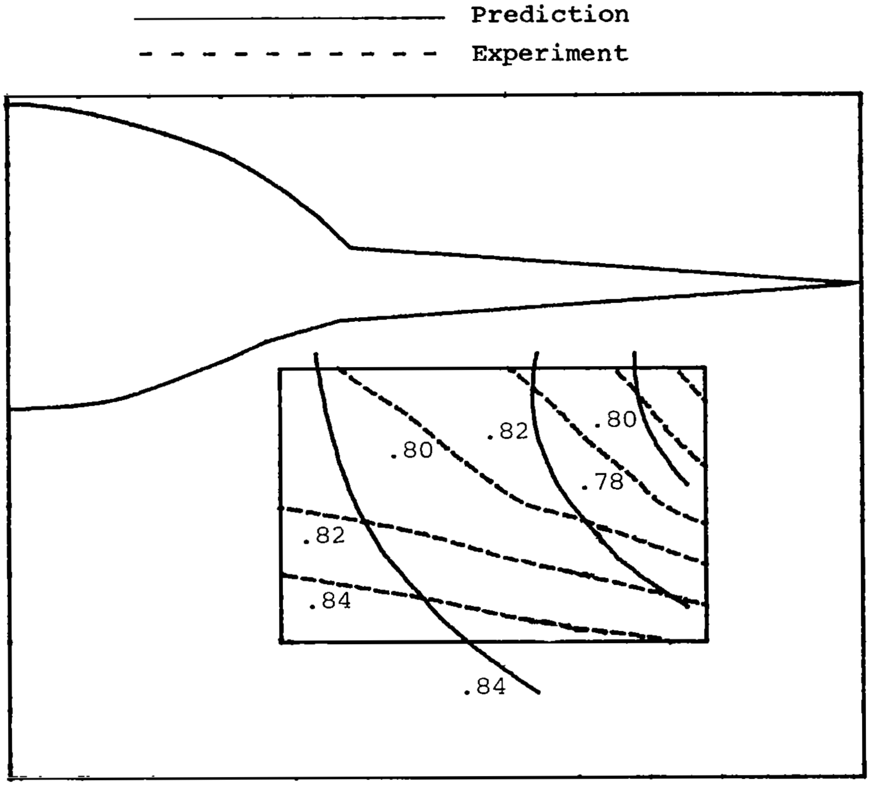

(c) M_l.

Figure 25.- Concluded.

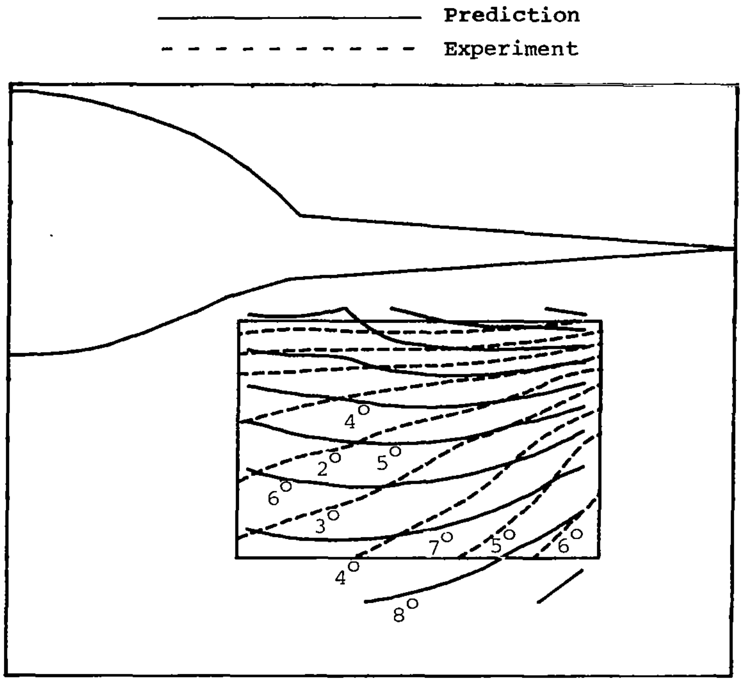

(a) α_l.

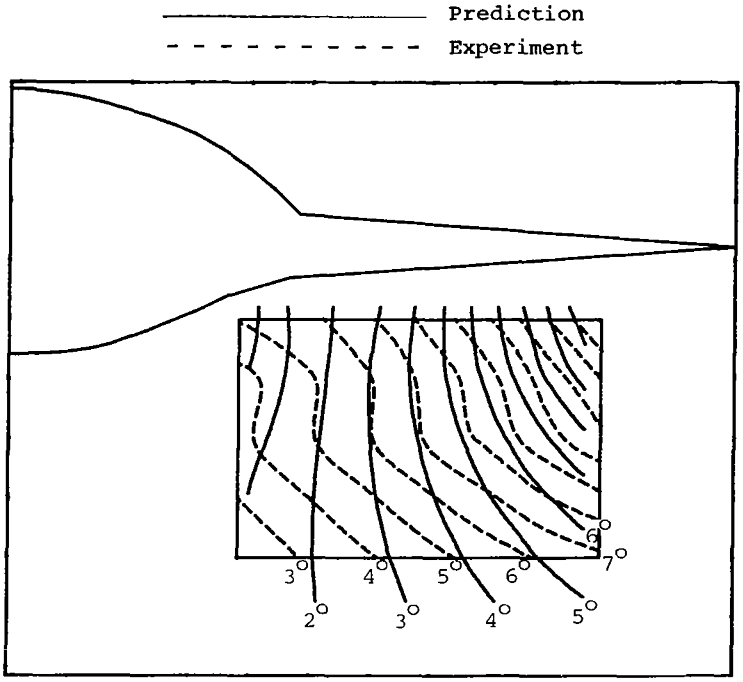

(b) β_l.

Figure 26.- Contours predicted from WIBCO code and Tailor-Mate experimental data for wing-shielded configuration at $M_\infty = 0.9$ and $\alpha = 15°$.

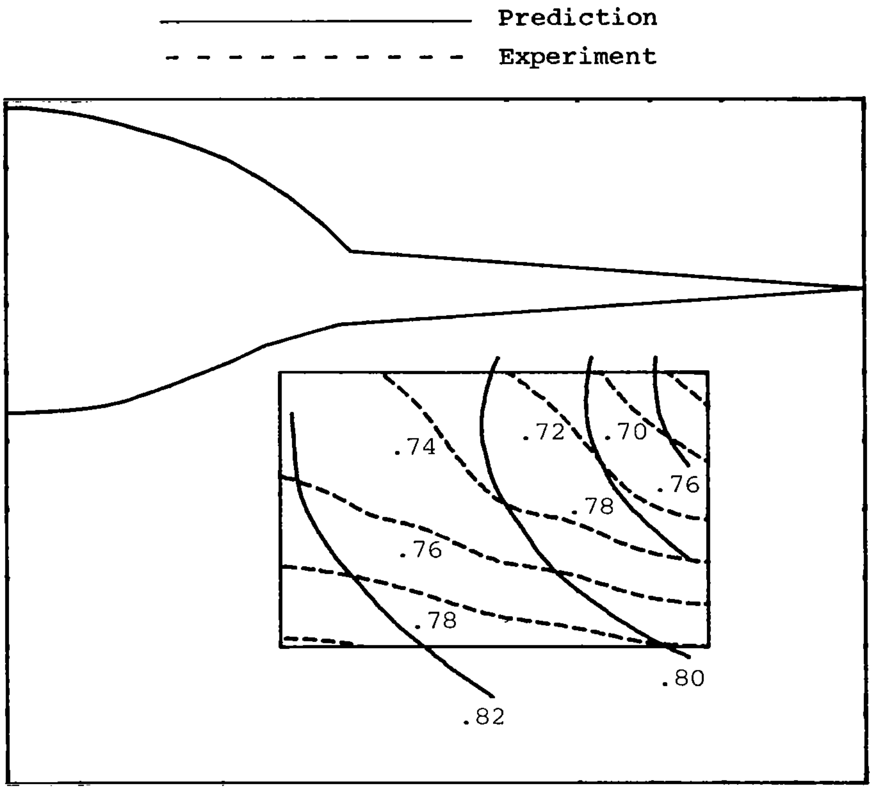

(c) M_l.

Figure 26.- Concluded.

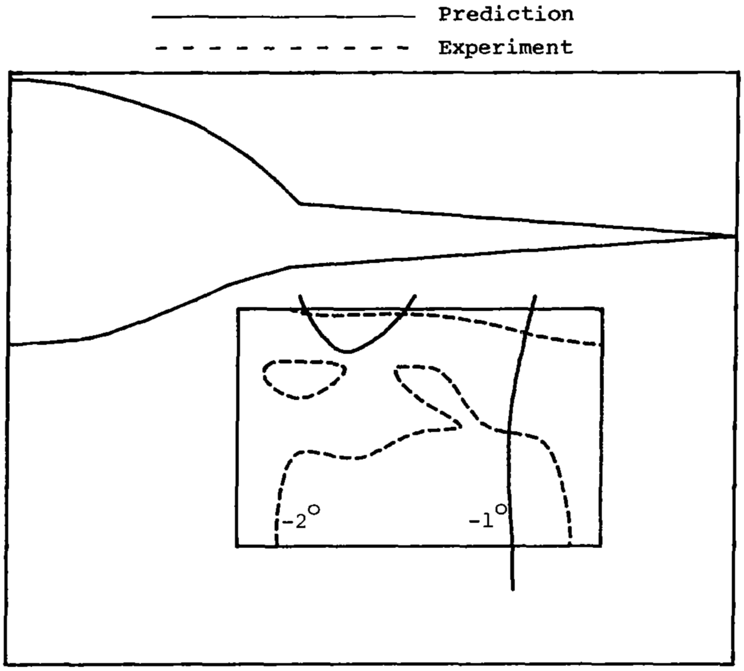

(a) α_l.

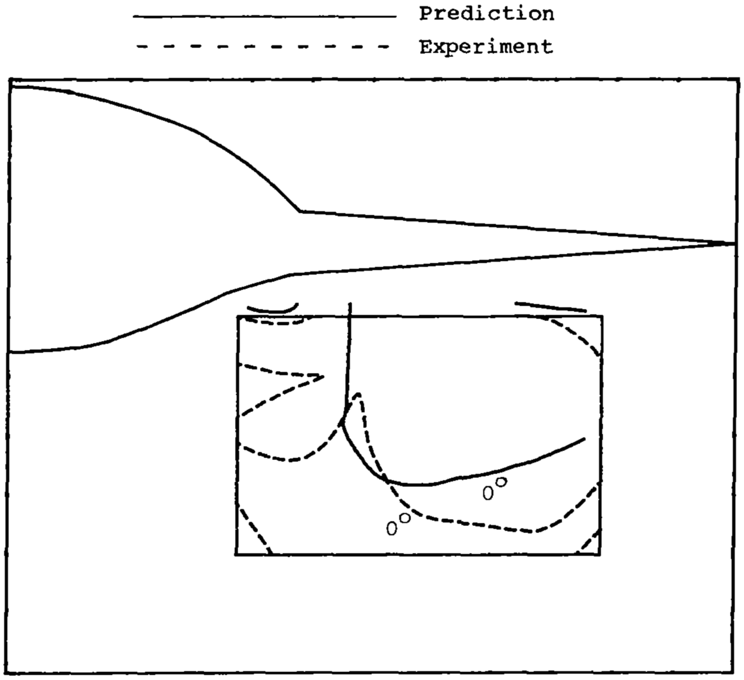

(b) β_l.

Figure 27.- Contours predicted from WIBCO code and Tailor-Mate experimental data for wing-shielded configuration at $M_\infty = 1.2$ and $\alpha = 0°$.

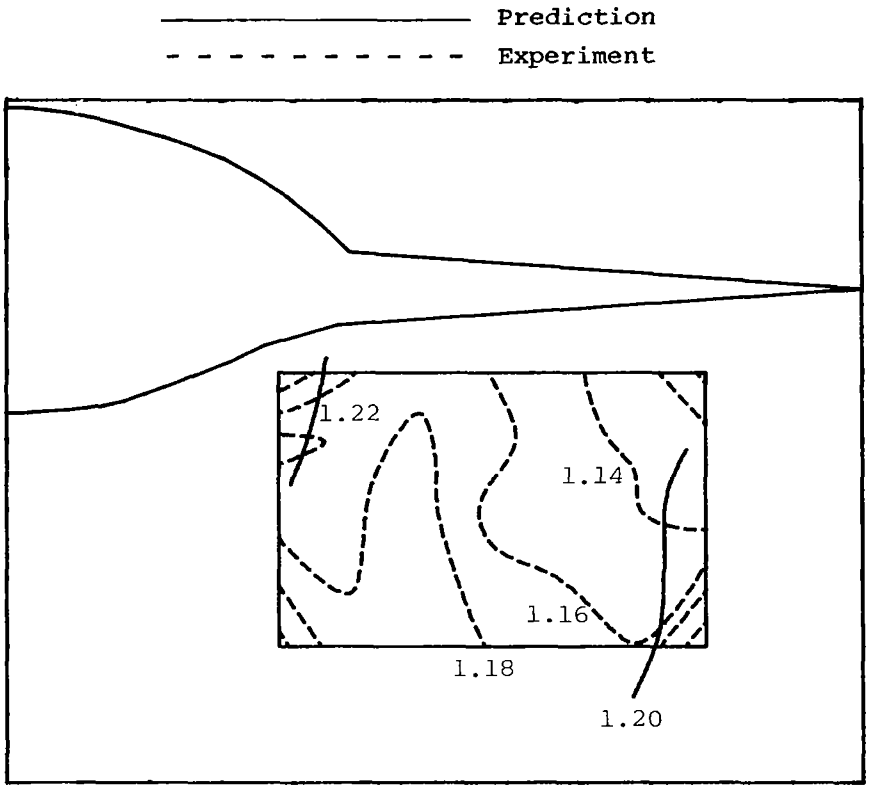

(c) M_l.

Figure 27.- Concluded.

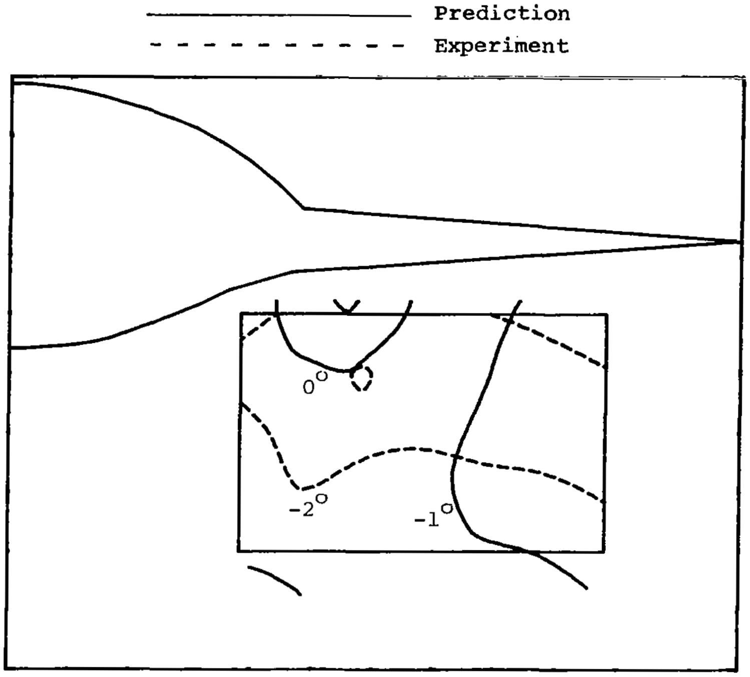

(a) α_l.

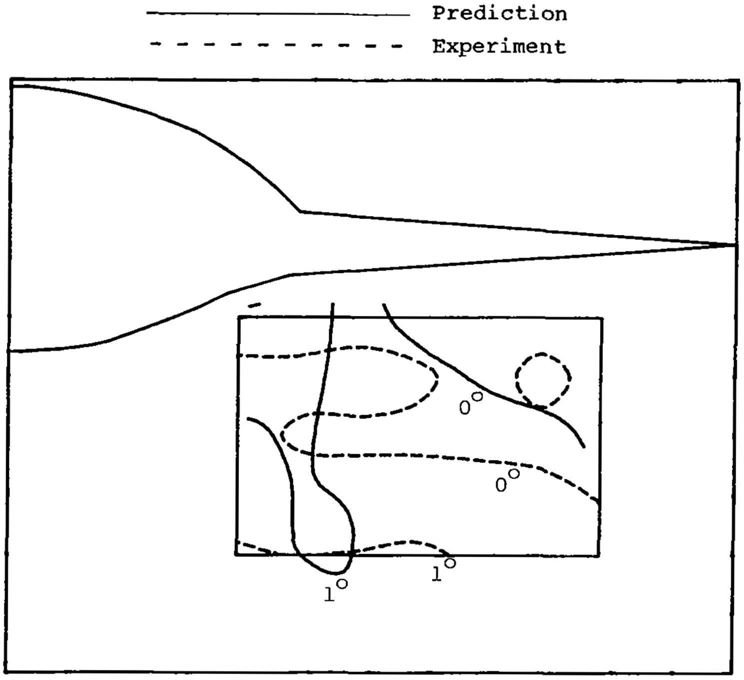

(b) β_l.

Figure 28.- Contours predicted from WIBCO code and Tailor-Mate experimental data for wing-shielded configuration at $M_\infty = 1.4$ and $\alpha = 0°$.

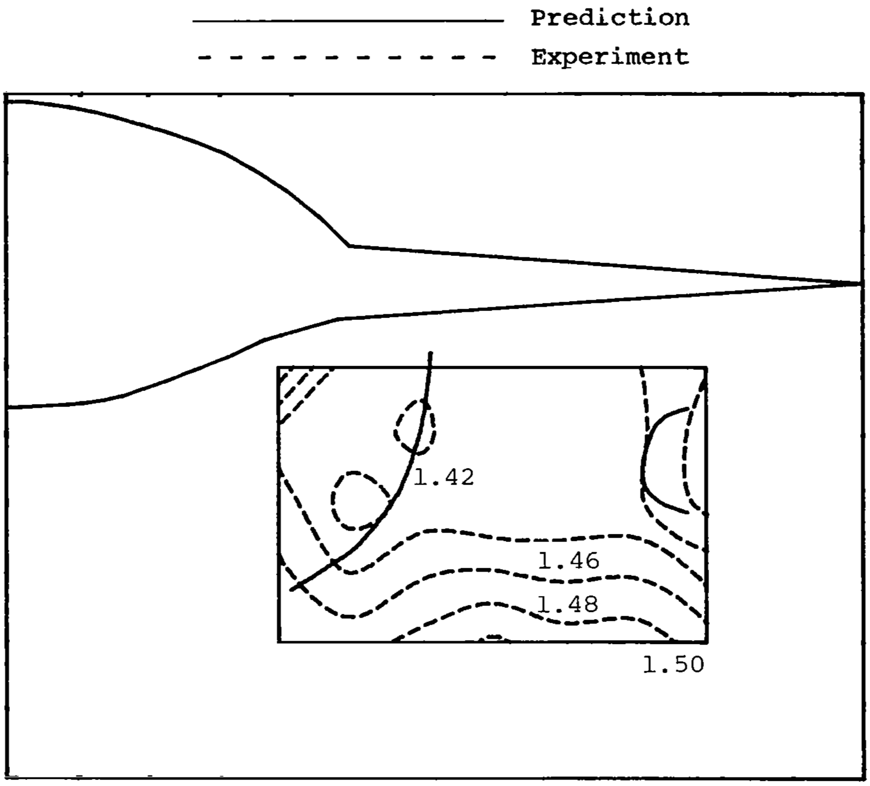

(c) M_l.

Figure 28.- Concluded.

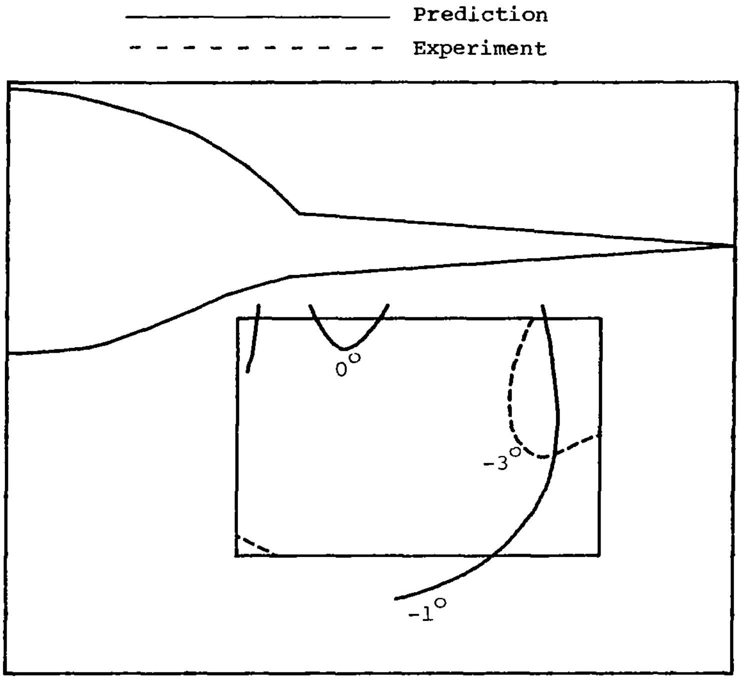

(a) α_l.

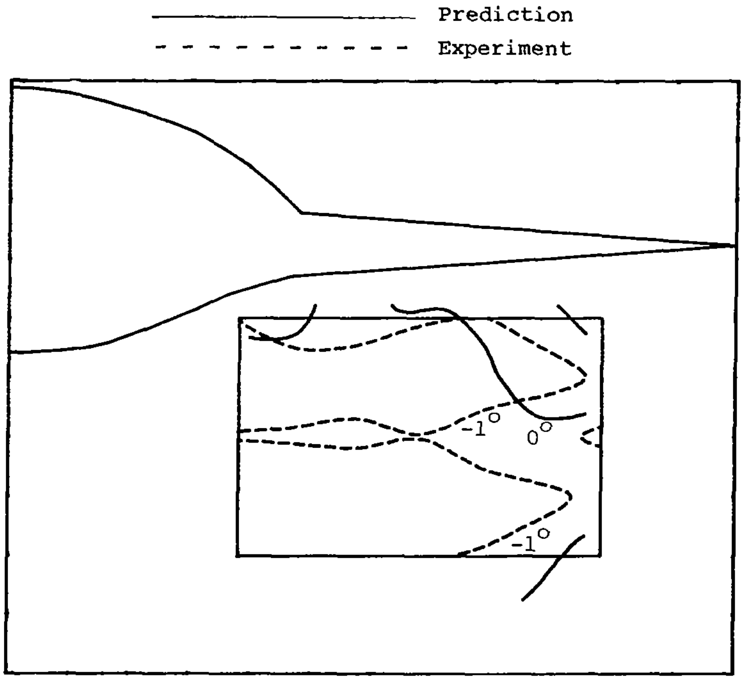

(b) β_l.

Figure 29.- Contours predicted from WIBCO code and Tailor-Mate experimental data for wing-shielded configuration at $M_\infty = 1.65$ and $\alpha = 0°$.

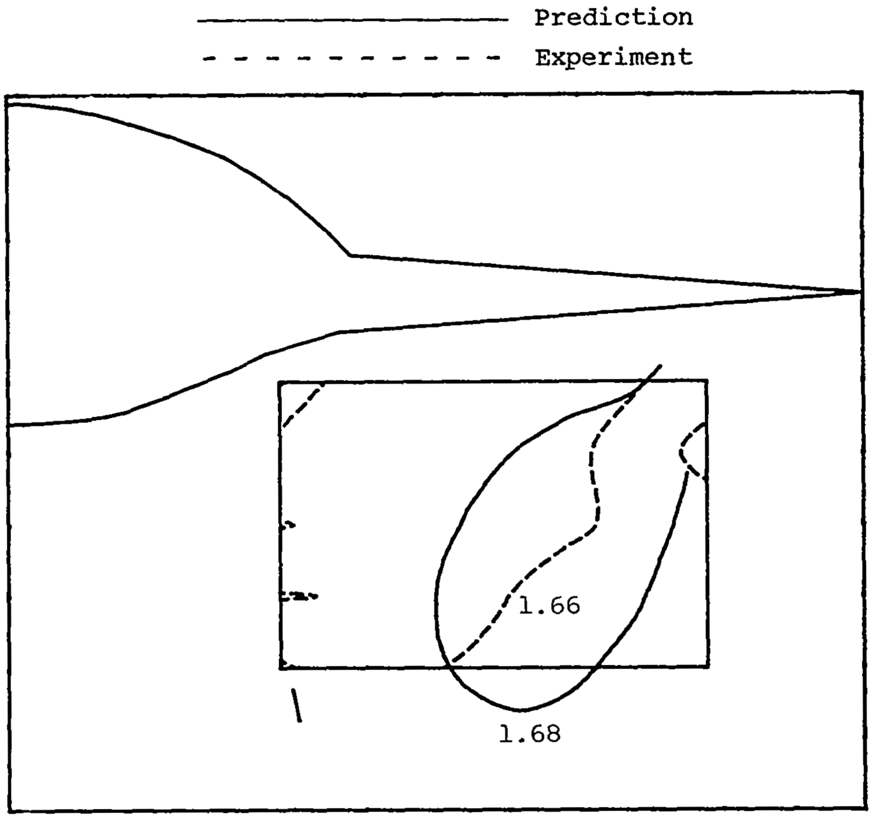

(c) M_l.

Figure 29.- Concluded.

1. Report No. NASA TP-2270	2. Government Accession No.	3. Recipient's Catalog No.

4. Title and Subtitle THEORETICAL AND EXPERIMENTAL ENGINE-INLET FLOW FIELDS FOR FIGHTER FOREBODIES	5. Report Date February 1984
	6. Performing Organization Code 505-31-23-08
7. Author(s) Steven F. Yaros	8. Performing Organization Report No. L-15639
9. Performing Organization Name and Address NASA Langley Research Center Hampton, VA 23665	10. Work Unit No.
	11. Contract or Grant No.
12. Sponsoring Agency Name and Address National Aeronautics and Space Administration Washington, DC 20546	13. Type of Report and Period Covered Technical Paper
	14. Sponsoring Agency Code

15. Supplementary Notes

16. Abstract

This investigation examined the capability of two numerical methods, one for transonic and one for supersonic flows, to predict the flow fields about representative fighter aircraft forebodies in the vicinity of the engine inlets. The Mach number range covered was 0.9 to 2.5 and the angle-of-attack range was 0° to 25°. The computer programs that implement each of the numerical methods are described as to their features and usage, and results are compared with comprehensive wind tunnel data. Although both prediction methods were inviscid, results show that the aerodynamic effects of the forebody, with and without a wing, can be simulated fairly well. Further work is needed to include the effects of viscosity, including vortex shedding.

17. Key Words (Suggested by Author(s)) Transonic flow Supersonic flow Fighter aircraft Forebody flow Inlet flow	18. Distribution Statement Unclassified - Unlimited Subject Category 02

19. Security Classif. (of this report)	20. Security Classif. (of this page)	21. No. of Pages	22. Price
Unclassified	Unclassified	64	A04

For sale by the National Technical Information Service, Springfield, Virginia 22161

NASA-Langley, 1984

National Aeronautics and
Space Administration

Washington, D.C.
20546

Official Business
Penalty for Private Use, $300

THIRD-CLASS BULK RATE

Postage and Fees Paid
National Aeronautics and
Space Administration
NASA-451

U.S.MAIL

1 1 1U,A, 840203 S00903DS
DEPT OF THE AIR FORCE
AF WEAPONS LABORATORY
ATTN: TECHNICAL LIBRARY (SUL)
KIRTLAND AFB NM 87117

S

NASA

POSTMASTER: If Undeliverable (Section 158
Postal Manual) Do Not Return